Journal of the Mechanics and Physics of Solids 131 (2019) 404–423

Contents lists available at ScienceDirect

Journal of the Mechanics and Physics of Solids

journal homepage: www.elsevier.com/locate/jmps

Effect of machine stiffness on interpreting contact force–indentation depth curves in adhesive elastic contact experiments

Weilin Deng, Haneesh Kesari*

School of Engineering, Brown University, Providence, RI 02912, United States

ARTICLE INFO

Article history:
Received 19 December 2018
Revised 21 June 2019
Accepted 11 July 2019
Available online 16 July 2019

Keywords:
Adhesion
Contact experiment
Machine stiffness
JKR
Pull-in instability
Pull-off instability
Hysteretic energy loss

ABSTRACT

Dry adhesion plays a critical role in many fields, including the locomotion of some insects and failure of microelectromechanical systems. The Dupré's work of adhesion of a contact interface is an important metric of dry adhesion. It is often measured by applying the Johnson–Kendall–Roberts (JKR) theory [1] to contact force–indentation depth curves that are measured using an atomic force microscope (AFM), or an instrument modeled after it. The JKR theory has been exceptionally successful in interpreting contact force–indentation depth measurements and explaining adhesive, elastic contact phenomena, such as the pull-in and pull-off instabilities. However, in many cases the JKR theory predicts a lower magnitude for the pull-off force than what is experimentally measured, and it does not capture the finite changes in the indentation depth that occur during the pull-in and pull-off instabilities. In those cases, applying the JKR theory to calculate the work of adhesion from only the measured pull-off force is likely to give highly inaccurate results. We believe that these discrepancies occur because the classical JKR theory ignores the machine stiffness—which, in the case of AFM-type instruments, is the stiffness of the mechanical structure that connects the tip to the translation stage, which moves the tip towards and away from the substrate. In this paper, we present a model that is related to, but more general than, the JKR theory that accounts for the machine stiffness. This model explains the experimental data better than the JKR theory in the cases where the JKR theory displays the aforementioned discrepancies. We consider both the first order necessary and the higher order sufficiency conditions while deriving the solutions in our model.

1. Introduction

Van der Waals (dipole–dipole) and Coulombic interactions between molecules can give rise to attractive forces between solids (Israelachvili, 2011; Kendall, 2001). These attractive forces can make a pair of contacting surfaces adhesive even when they are not connected by any liquid bridges. The effect of these attractive forces, termed *dry adhesion*, operates at all scales but is dominant at μm–nm lengths (Fig. 1a).

Dry adhesion has been found to play an important role in many fields, including biology, engineering, and physics. Many insects, spiders, and reptiles, for example, possess fibrillar structures on their foot pads that, through adhesion, allow these

* Corresponding author.
E-mail address: haneesh_kesari@brown.edu (H. Kesari).

https://doi.org/10.1016/j.jmps.2019.07.009
0022-5096/

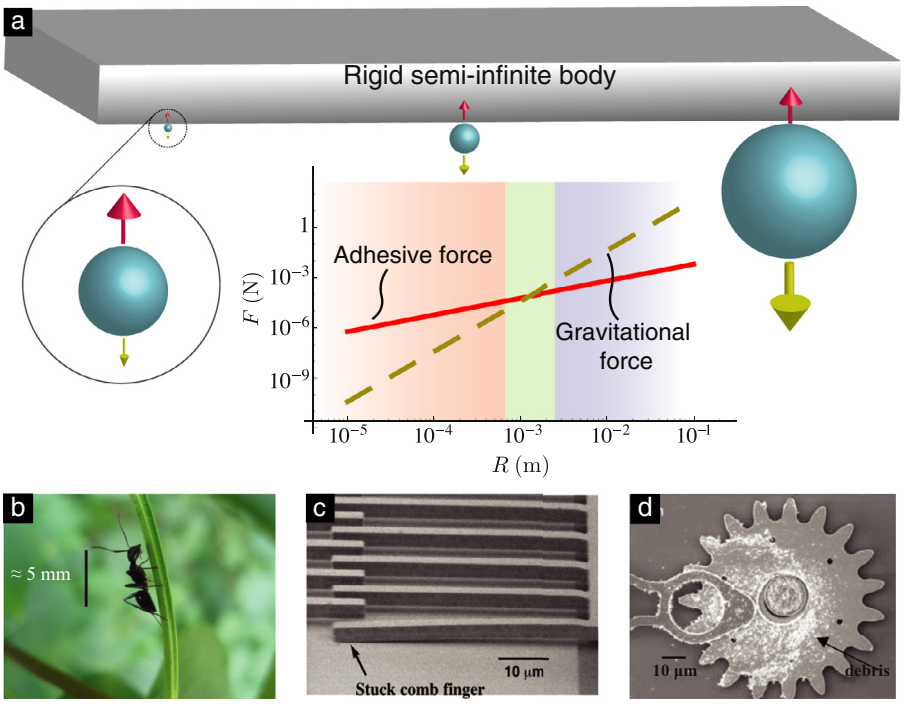

Fig. 1. (a) Adhesion dominates at small scales. Bradley (1932) considered the adhesive force between a rigid sphere and a rigid semi-infinite body. He assumed that the adhesive interaction between two molecules of the solids, with centers a distance d apart, is proportional to $1/d^n$ where n is an integer. The adhesive force is found to be $2\pi wR$, where w is the work of adhesion and R is the radius of the sphere. At the same time, the gravitational force on the sphere is $4\pi\rho gR^3/3$ where ρ is the density of the material of which the sphere is composed. For most engineering materials, w and ρ are of the order of 10 mJ/m^2 (Maugis, 2000) and 10^3 kg/m^3, respectively. (b) An ant climbs on a plant stem, showcasing that adhesive forces overcomes the gravitational forces at small length scales. (c) A comb finger of a drive actuator is stuck to the substrate due to adhesion (Tanner et al., 2000). (d) Wear debris accumulates on the surface of the gear of a microengine (Tanner et al., 2000) as a result of adhesion.

animals to adeptly scale vertical surfaces (Arzt et al., 2003; Bullock and Federle, 2011; Eisner and Aneshansley, 2000; Frost et al., 2018; Huber et al., 2007; Wolff and Gorb, 2012) (Fig. 1b). In microelectromechanical systems (MEMS) engineering, adhesion-induced device failure is a pervasive problem that limits its continued development. In MEMS devices, such as comb drive accelerometers, slender, micrometer-sized structures are aligned in parallel rows in close proximity to one another (Fig. 1c). During the device's fabrication stage or later in its operation, these structures can unintentionally come into contact with each other or the substrate and remain permanently adhered, leading to device failure (Tanner et al., 2000). Adhesion also plays a role in the physical properties that underlie friction and wear at the sub-micrometer scale (Friedrich, 2012; Hutchings and Shipway, 2017). Contact between hard solids, such as metals and ceramics, primarily takes place at the surfaces' asperities. Adhesion firmly welds the asperities, and thus the two solids. In order to move or slide the solids over one another, significant frictional force must be generated in order to break the asperities apart or rupture the asperities from their respective solids, contributing to wear (Fig. 1d).

An important metric for quantifying dry adhesion between two contacting solids is the Dupré's work of adhesion,

$$w := \gamma_1 + \gamma_2 - \gamma_{12}, \tag{1.1}$$

where γ_1 and γ_2 are the surface energies of the two solids and γ_{12} is the contact interface's energy per unit area (Maugis, 2000). Adhesion can be measured through a variety of tests and experiments, including thin film peeling (Cohen et al., 2018; Kendall, 1971; Kim et al., 1989), blister tests (Cao et al., 2014; Hinkley, 1983), and normal contact experiments (Ahn and Shull, 1996; Bouchonville et al., 2016; Deng and Kesari, 2019; Ebenstein and Pruitt, 2006; Ebenstein and Wahl, 2006; Kesari et al., 2010; Notbohm et al., 2012; Sun et al., 2004). Among these techniques, normal contact experiments distinguish themselves for two reasons: firstly, they can provide information about the materials' elastic properties; and secondly, they can spatially map out a material's surface adhesive and bulk elastic properties at the μm–nm length scales, making it the preferred test for evaluating adhesion and the elasticity of a solid.

Normal contact experiments are typically performed using an atomic force microscope (AFM) (Bouchonville et al., 2016; Ebenstein and Wahl, 2006; Kesari et al., 2010; Notbohm et al., 2012; Sun et al., 2004) or an instrument modeled after it. In these experiments, a sample of the material whose properties are to be examined is prepared in the form of a rectangular or circular slab. This slab is most commonly referred to as the substrate. The substrate is placed under a rigid tip, which is connected to a stage via a passive mechanical structure, such as the cantilever in an AFM (Fig. 2a). The instrument controls

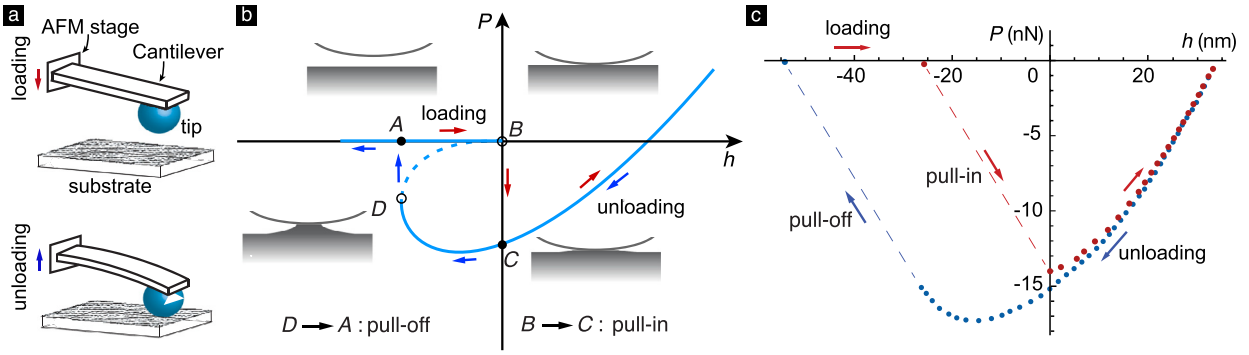

Fig. 2. (a) A schematic of an AFM contact experiment. The instrument brings the tip and substrate into and out of contact by controlling the position of the stage, which is connected to the tip by an elastic cantilever. (b) The contact force–indentation depth curve according to the JKR theory. The pull-in instability ($B \to C$) and pull-off instability ($D \to A$) are marked along with corresponding contact configurations. (c) The measured contact force–indentation depth data from the contact experiments between a glass bead and a Polydimethylsiloxane (PDMS) substrate (Sun et al., 2004).

the position of the stage and brings the tip and substrate into and out of contact. Mechanical properties are measured at a given location on a substrate's surface by carrying out one or more contact cycles. Each contact cycle begins with a loading phase, when the stage moves towards the substrate, followed by an unloading phase, when the stage moves away from the substrate. During contact cycles, the deformation of the mechanical structure that connects the stage to the tip is often small, resembling an elastic spring. The stiffness of this spring is referred to as the *machine stiffness*. In AFM contact experiments, the mechanical structure that connects the tip to the stage is a cantilever. The cantilever's shape, size, and material composition then dictate the machine stiffness.

In the experiments, the contact force that arises between the two solids is measured as a function of the indentation depth which is the distance from the undeformed substrate's surface to the tip. The properties of the substrate are obtained from the contact force–indentation depth data based on a classical adhesive contact theory such as the Johnson–Kendall–Roberts (JKR) theory (Johnson et al., 1971). According to the JKR theory, the tip would jump into contact with the substrate unstably in the loading phase, resulting in an abrupt decrease in the contact force. Similarly, in the unloading phase, the tip would jump out of contact with the substrate spontaneously, resulting in a sudden increase in contact force. The phenomena of the tip jumping into and out of contact with the substrate unstably are called *pull-in* and *pull-off* instabilities, respectively. There are two important experimental results that differ from the JKR predictions. First, the indentation depth just before and after the pull-in and pull-off instabilities do not change as per the JKR theory, see Fig. 2b. However, in many adhesive contact experiments the indentation depth just before and after the pull-in and pull-off instabilities are different (Ebenstein and Wahl, 2006; Kesari et al., 2010; Notbohm et al., 2012; Sun et al., 2004), see Fig. 2c. Second, the JKR theory predicts the contact force at the pull-off instability, i.e., the pull-off force, to be $-5\pi wR/6$, where R is the radius of curvature of the tip; whereas the measured pull-off force in experiments is different from that value (see Section 4). The work of adhesion would be inaccurate if it were calculated using the pull-off force given by the JKR theory. The reason for this difference is due to the machine stiffness, whose effect is overlooked in the JKR theory.

In this paper, we show that machine stiffness is an important factor in adhesive contact. Our problem is a model for a class of contact experiments that are conducted using an AFM-type instrument. We consider an axisymmetric mechanics problem involving the adhesive, frictionless contact between two solids to study the effect of machine stiffness. Both the tip's symmetry axis and the stage's translational directions are normal to the substrate's surface that faces the tip. We assume that the contact region is simply connected and hence is a disk that has its center on the tip's symmetry axis. Just as in the JKR model (Johnson et al., 1971), adhesion in our problem is modeled as an infinitesimal interaction—albeit its origins from the van der Waals and Coulombic interactions are finite-ranged. More specifically, Johnson et al. (1971) treated adhesive elastic contact by including an adhesion energy term in the system's total potential energy, and then determined the contact region by stipulating that the contact radius locally minimizes the potential energy. We adopt the same methodology as Johnson et al. (1971), and additionally include an elastic energy term that results from the deformation of the instrument's mechanical structure into the total potential energy calculation of our model. We use a variational approach in the study of our adhesive contact problem and derive the necessary and sufficient conditions on the solutions to our problem. We remark that Takahashi et al. (1995) and Yang (2003) analyzed the effect of machine stiffness on the adhesive contact between a paraboloidal tip and an elastic half-space. They too use a variational approach. However, our approach is different from that of Takahashi et al. and Yang in that they only consider the first order necessary conditions on the solutions to their problems, while in our model we further consider the second order sufficiency conditions on the solutions. Second order sufficiency conditions have previously been used to study the stability of the equilibrium configurations in adhesive elastic contact problems by Kesari and Lew (2011), Argatov et al. (2016), Willert et al. (2016), and Popov et al. (2017), among others.

The outline of the paper is as follows. First, we formulate our contact problem using the variational approach and derive the solutions in Section 2. In Section 3 we consider two tip geometries, spherical and conical, as examples to illustrate

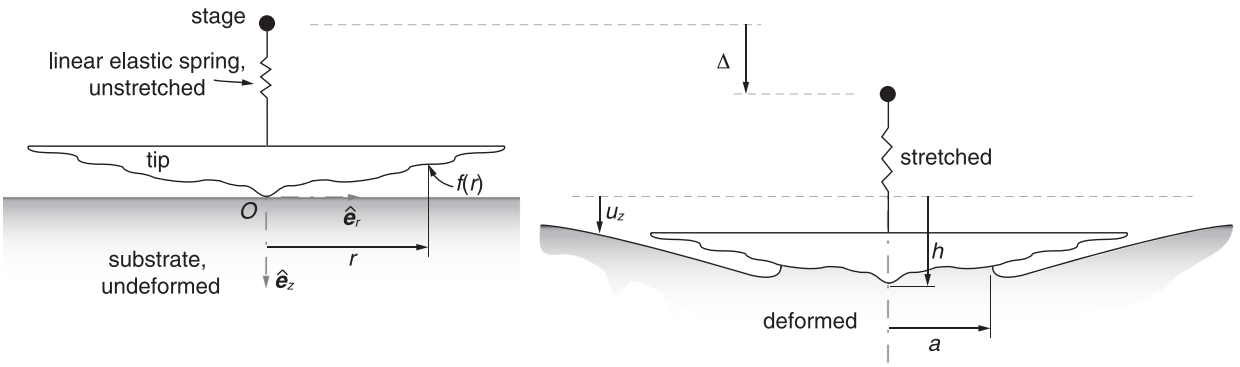

Fig. 3. (a) and (b), respectively, show the reference and a deformed configuration of the contacting solids in our problem, see Section 2.1.

the results derived in Section 2. In this section, we also study the dependence of the pull-in and pull-off instabilities and the resulted hysteretic energy loss on the machine stiffness. We compare the theoretical predictions of our model with experimental measurements and discuss some potential sources for the discrepancies between our model and experiments in Section 4.

2. Adhesive elastic contact model

2.1. Geometry

Fig. 3 shows the geometry of our contact mechanics problem. Our problem has the three-dimensional Euclidean point space $\mathbb{E}^3$ as its backdrop. We identify points in $\mathbb{E}^3$ using the set of Cartesian coordinates $\{x, y, z\}$ that correspond to a fixed, orthonormal set of vectors $\{\hat{\boldsymbol{e}}_x, \hat{\boldsymbol{e}}_y, \hat{\boldsymbol{e}}_z\}$ that span the vector space $\mathcal{V}$ associated with $\mathbb{E}^3$.

The tip in the class of experiments that we model in this paper is usually composed of materials that are much stiffer than that of the substrate. Thus, we model the tip as a rigid solid. Recall that in the experiments we model, the tip's geometry has continuous rotational symmetry. Therefore, we take the tip to be a solid of revolution whose symmetry axis is a fixed line that is parallel to $\hat{\boldsymbol{e}}_z$ and passes through the fixed point o, which is the origin of $\mathbb{E}^3$. In the reference configuration of our problem (Fig. 3a), the tip's surface facing the substrate is the region

$$\partial\mathcal{T}_0 := \{\mathcal{P}_t = o + r\hat{\boldsymbol{e}}_r(\theta) + f(r)\hat{\boldsymbol{e}}_z \in \mathbb{E}^3 \mid \theta \in [0, 2\pi) \text{ and } r \in [0, \infty)\},$$

where the tip's radial profile $f : [0, \infty) \to (-\infty, 0]$ is a sufficiently smooth function such that $f(0) = 0$, the vector $\hat{\boldsymbol{e}}_r(\theta) := \cos\theta\hat{\boldsymbol{e}}_x + \sin\theta\hat{\boldsymbol{e}}_y$, and r and θ are, respectively, the radial and polar coordinates of $\mathcal{P}_t$.

We model the instrument's stage as a material point and the structure connecting the tip and the stage as a linear elastic spring. In the reference configuration of Fig. 3a, the spring is unstretched. In the class of experiments we model, the size of the contact region is typically much smaller than the dimensions of the substrate. In the reference configuration, the substrate occupies the region $z \geq 0$, which we refer to as the half-space $\mathcal{S}_0$. We refer to the surface of $\mathcal{S}_0$ that faces the tip as $\partial\mathcal{S}_0$. In the reference configuration, there is no contact between the tip and substrate and the substrate is stress-free. We discuss in more detail what it means for the tip and substrate to be in contact later in this section.

Fig. 3b shows the deformed configuration of our problem. In it, the stage and tip have been moved by amounts of $\Delta\hat{\boldsymbol{e}}_z$ and $h\hat{\boldsymbol{e}}_z$, respectively, from where they were located in the reference configuration. We call Δ the stage displacement and $h \in (-\infty, +\infty)$ the indentation depth. In the deformed configuration, the tip's surface facing the substrate occupies the region

$$\partial\mathcal{T}_t := \{o + r\hat{\boldsymbol{e}}_r(\theta) + \tilde{u}_z(r; h)\hat{\boldsymbol{e}}_z \in \mathbb{E}^3 \mid \theta \in [0, 2\pi) \text{ and } r \in [0, \infty)\},$$

where $\tilde{u}_z(\cdot, h) : [0, \infty) \to (-\infty, +\infty)$ is defined as

$$\tilde{u}_z(r; h) := h + f(r). \tag{2.1}$$

As is standard in continuum mechanics, we identify material particles that belong to the tip or substrate by the spatial points in the reference configuration $\mathbb{E}^3$ where they originate. We say that a substrate's surface material particle $\mathcal{S} \in \partial\mathcal{S}_0$ is a contact particle if there exists a tip material particle $\mathcal{Q} \in \partial\mathcal{T}_0$ such that $\mathcal{S}$ and $\mathcal{Q}$ occupy the same spatial point in the deformed configuration. We refer to the set of all contact particles as the contact region Γ_c and to the measure of Γ_c as the contact area. We define the tip and substrate to be in contact if the contact area is strictly positive. As previously noted, our problem is axisymmetric and the contact region in it is simply connected. Therefore, we can always write $\Gamma_c = \{\mathcal{S} \in \partial\mathcal{S}_0 \mid r \leq a\}$, where r is $\mathcal{S}$'s radial coordinate and $a \geq 0$ is Γ_c's contact radius.

Let $\mathcal{P} \in \mathcal{S}_0$ be a substrate material particle. The displacement of $\mathcal{P}$ is the vector $\boldsymbol{u}(\mathcal{P})$ that is defined such that $\mathcal{P} + \boldsymbol{u}(\mathcal{P}) = p$, where p is $\mathcal{P}$'s location in the deformed configuration. In our problem we only consider displacement fields $\boldsymbol{u} : \mathcal{S}_0 \to \mathcal{V}$

for which p has the same θ coordinate as $\mathcal{P}$. Therefore, $\boldsymbol{u}(\mathcal{P})$ can be expressed as $u_r(r,z)\hat{\boldsymbol{e}}_r(\theta)+u_z(r,z)\hat{\boldsymbol{e}}_z$, where r, θ, and z are $\mathcal{P}$'s cylindrical coordinates and $u_r(\cdot,\cdot),\ u_z(\cdot,\cdot):[0,\infty)\times[0,\infty)\to(-\infty,\infty)$.

Let $\mathcal{S}\in\partial\mathcal{S}_0$ be a contact particle that is in contact with a tip particle $\mathcal{Q}\in\partial\mathcal{T}_0$. Because $\mathcal{S}$ and $\mathcal{Q}$ occupy the same spatial point in the deformed configuration, it follows that

$$(r_{\mathcal{S}}+u_r(r_{\mathcal{S}},0))\hat{\boldsymbol{e}}_r(\theta_{\mathcal{S}})+u_z(r_{\mathcal{S}},0)\hat{\boldsymbol{e}}_z=r_{\mathcal{Q}}\hat{\boldsymbol{e}}_r(\theta_{\mathcal{Q}})+\tilde{u}_z(r_{\mathcal{Q}};h)\hat{\boldsymbol{e}}_z, \tag{2.2}$$

where $r_{\mathcal{S}}$, $\theta_{\mathcal{S}}$ and $r_{\mathcal{Q}}$, $\theta_{\mathcal{Q}}$ are the radial and polar coordinates of $\mathcal{S}$ and $\mathcal{Q}$, respectively. It follows from (2.2) that $\theta_{\mathcal{S}}=\theta_{\mathcal{Q}}$, $r_{\mathcal{S}}+u_r(r_{\mathcal{S}},0)=r_{\mathcal{Q}}$, and

$$u_z(r_{\mathcal{S}},0)=\tilde{u}_z(r_{\mathcal{S}}+u_r(r_{\mathcal{S}},0);h). \tag{2.3}$$

Imposing the boundary condition (2.3) on the substrate's displacement field leads to a problem for which obtaining an analytical solution is quite challenging. In our problem, we impose the boundary condition

$$u_z(r_{\mathcal{S}},0)=\tilde{u}_z(r_{\mathcal{S}};h), \tag{2.4}$$

which is an approximation of (2.3) on the substrate's displacement field.

2.2. Variational formulation of the adhesive elastic contact problem

We use a variational perspective in the study of our contact mechanics problem. That is, for a given stage displacement Δ, we posit that the experimentally observed configuration of the spring, tip, and half-space is one in which the system's total energy is locally minimized with respect to a, h, and $\boldsymbol{u}$. Thus, we allow for the possibility of there being more than one configuration that is experimentally observable at a given Δ. We assume that the type of solutions we seek can be obtained by first minimizing the potential energy with respect to $\boldsymbol{u}$ alone, while holding a and h fixed, and then minimizing this partially minimized potential energy with respect to a and h.

The potential energy in our problem consists of three terms: the energy stored in the spring because of its stretching, the energy stored in the contact region due to the adhesive interactions between the tip and the substrate, and the energy stored in the substrate due to its deformation. The potential energy stored in the spring that connects the tip to the stage is $k_s(\Delta-h)^2/2$, where $k_s\in(0,\infty)$ is the spring's stiffness. As previously noted, we model adhesion between the tip and the substrate using the JKR theory. According to this theory, the potential energy from the adhesive interactions between the tip and substrate is $-\pi w a^2$. We model the substrate as a homogeneous, isotropic, linear elastic material with Young's modulus E and Poisson's ratio ν. Therefore, the potential energy stored in the substrate is

$$\frac{1}{2}\int_{\mathcal{S}_0}\boldsymbol{\sigma}:\boldsymbol{\epsilon}\,d\mathcal{S}_0, \tag{2.5}$$

where

$$\boldsymbol{\sigma}=\frac{E}{(1+\nu)}\left[\boldsymbol{\epsilon}+\frac{\nu}{(1-2\nu)}\mathrm{Tr}(\boldsymbol{\epsilon})\mathbf{I}\right] \tag{2.6}$$

is the Cauchy stress tensor and

$$\boldsymbol{\epsilon}=\frac{1}{2}\left(\nabla\boldsymbol{u}+\nabla\boldsymbol{u}^{\mathsf{T}}\right) \tag{2.7}$$

is the small strain tensor. The symbol: in (2.5) denotes double contraction. In (2.6), the symbol $\mathbf{I}$ denotes the second rank identity tensor and $\mathrm{Tr}(\cdot)$ denotes the trace operator. In (2.7) the operators $\nabla(\cdot)$ and $(\cdot)^{\mathsf{T}}$ denote the gradient and transpose operators, respectively.

It follows from (2.4) that the displacement field always needs to satisfy the essential boundary condition

$$u_z(r,0)=\tilde{u}_z(r;h)\quad\text{on}\quad\Gamma_c. \tag{2.8}$$

When Δ, a, and h are held fixed, it can be shown that among the displacement fields that satisfy (2.8), the one that minimizes the system's potential energy is the one that satisfies the equation and boundary conditions

$$\mathrm{Div}(\boldsymbol{\sigma})=\boldsymbol{o}\quad\text{in}\quad\mathcal{S}_0, \tag{2.9a}$$

$$\boldsymbol{\sigma}\hat{\boldsymbol{e}}_z=\boldsymbol{o}\quad\text{on}\quad\partial\mathcal{S}_0\backslash\Gamma_c, \tag{2.9b}$$

$$(\boldsymbol{I}-\hat{\boldsymbol{e}}_z\otimes\hat{\boldsymbol{e}}_z)\boldsymbol{\sigma}\hat{\boldsymbol{e}}_z=\boldsymbol{o}\quad\text{on}\quad\Gamma_c, \tag{2.9c}$$

where $\mathrm{Div}(\cdot)$ is the divergence operator, $\boldsymbol{o}$ is the null vector in $\mathcal{V}$, and $\hat{\boldsymbol{e}}_z\otimes\hat{\boldsymbol{e}}_z$ is the tensor product of $\hat{\boldsymbol{e}}_z$ and itself. It is also required that the components of $\boldsymbol{u}$ and $\boldsymbol{\sigma}$, respectively, be asymptotic to $(r^2+z^2)^{-1/2}$ and $(r^2+z^2)^{-1}$ as $(r^2+z^2)^{1/2}\to\infty$.

The solution to the mixed boundary value problem defined by (2.8) and (2.9) was given by Sneddon (1965). (For a concise derivation of this solution using Betti's reciprocity theorem, see Kesari and Lew (2012).) Using that solution, it can be shown that for any given Δ and h and a positive a, the partially minimized potential energy of the system is

$$\frac{\pi^2E}{4(1-\nu^2)}\int_0^a\chi(\tilde{a};h)^2\,d\tilde{a}+\frac{1}{2}k_s(\Delta-h)^2-\pi w a^2, \tag{2.10}$$

where

$$\chi(\tilde{a};h)=\frac{2}{\pi}\left[h+\tilde{a}\int_0^{\tilde{a}}\frac{\tilde{u}_z'(r;h)}{\sqrt{\tilde{a}^2-r^2}}\,dr\right]\quad\text{for}\quad\tilde{a}>0. \tag{2.11}$$

Because of the boundary condition (2.8), the mixed boundary value problem defined by is not well posed when $a=0$ and $h\neq 0$. The value of the expression (2.10) equals the system's partially minimized potential energy only when $a>0$ or when $a=0$ and $h=0$. When $a=0$ and $h\leq 0$, the tip and the half-space are not in contact. In this case, the partially minimized potential energy only results from the stretching or compression of the spring. It is not possible for $a=0$ and $h>0$ because the tip cannot move into the region that is occupied by the unstressed half-space without forming any contact area with the half-space. Therefore, we conclude that the variational solution we seek will remain unaltered if we take the partially minimized potential energy of the system to be given by the value of the function $\Pi(\cdot,\cdot;\Delta):\mathcal{D}\subset\mathbb{R}^2\to\mathbb{R}\cup+\infty$, where

$$\Pi(a,h;\Delta):=\begin{cases}\frac{\pi^2\mathcal{E}}{4}\int_0^a\chi(\tilde{a};h)^2\,d\tilde{a}+\frac{1}{2}k_s(\Delta-h)^2-\pi wa^2, & a>0,\ h\in(-\infty,+\infty),\\ \frac{1}{2}k_s(\Delta-h)^2, & a=0,\ h\leq 0,\\ +\infty, & a=0,\ h>0,\end{cases} \tag{2.12}$$

with the domain

$$\mathcal{D}:=[0,\infty)\times(-\infty,+\infty), \tag{2.13}$$

and the plane strain Young's modulus $\mathcal{E}:=E/(1-\nu^2)$. We next locally minimize $\Pi(\cdot,\cdot;\Delta)$ with respect to a and h. More precisely, we seek the solution point $(a^*,h^*)\in\mathcal{D}$ for which there exists a positive number δ such that

$$\Pi(a^*,h^*;\Delta)\leq\Pi(a,h;\Delta),\quad\forall(a,h)\ \in\ B(a^*,h^*,\delta), \tag{2.14}$$

where $B(a^*;h^*;\delta):=\{(a,h)\in\mathbb{R}^2|\ \|(a^*,h^*)-(a,h)\|<\delta\}$. The solution point is also said to be the stable equilibrium configuration of the adhesive elastic contact.

2.3. Solutions

2.3.1. Contact radius and indentation depth

The solutions defined by (2.14) can lie either in the interior of the domain or on its boundary. We name the points in the interior of $\mathcal{D}$ *interior points* and on the boundary of $\mathcal{D}$ *boundary points*. We denote the boundary of $\mathcal{D}$ as $\text{int}(\mathcal{D})$ and the interior of $\mathcal{D}$ as $\partial\mathcal{D}$. It follows from the definition of $\mathcal{D}$ that the interior and boundary points are simply the points $(a,h)\in\mathbb{R}^2$ with $a>0$ and $a=0$, respectively. We show in Appendix A that the boundary contains solutions only when $\Delta<0$, and that those solutions are of the form $(0,\Delta)$. In the remainder of this section, we only discuss solution points that lie in $\text{int}(\mathcal{D})$. We begin by defining and characterizing the stationary points that are relevant for our discussion of interior solution points.

Stationary points. A stationary point (a°,h°) is an interior point that satisfies the first order conditions

$$\frac{\partial\Pi}{\partial h}(a^\circ,h^\circ;\Delta)=0, \tag{2.15a}$$

$$\frac{\partial\Pi}{\partial a}(a^\circ,h^\circ;\Delta)=0. \tag{2.15b}$$

The stationary point is also referred to as the equilibrium configuration of the adhesive elastic contact. At all interior points (a,h) it follows from (2.12) that

$$\frac{\partial\Pi}{\partial h}(a,h;\Delta)=\frac{\pi^2\mathcal{E}}{2}\int_0^a\chi(\tilde{a};h)\frac{\partial\chi(\tilde{a};h)}{\partial h}\,d\tilde{a}-k_s(\Delta-h), \tag{2.16a}$$

$$\frac{\partial\Pi}{\partial a}(a,h;\Delta)=\frac{\pi^2\mathcal{E}}{4}\chi(a;h)^2-2\pi aw. \tag{2.16b}$$

At any interior point (a,h) it follows from (2.11) that $\partial\chi(a;h)/\partial h=2/\pi$. Thus, after substituting $\partial\chi(\tilde{a};h)/\partial h$ with $2/\pi$ in (2.16a) and simplifying, we find that

$$\frac{\partial\Pi}{\partial h}(a,h;\Delta)=\pi\mathcal{E}\int_0^a\chi(\tilde{a};h)\,d\tilde{a}-k_s(\Delta-h). \tag{2.17}$$

Eqs. (2.15a) and (2.17) imply that

$$\pi\mathcal{E}\int_0^{a^\circ}\chi(\tilde{a};h^\circ)\,d\tilde{a}-k_s(\Delta-h^\circ)=0. \tag{2.18}$$

Eqs. (2.15b) and (2.16b) imply that $\chi(a^\circ; h^\circ)$ is equal to $\pm\sqrt{8a^\circ w/(\pi \mathcal{E})}$. However, we show in Appendix B that only the negative square root is physically meaningful, i.e.,

$$\chi(a^\circ; h^\circ) = -\sqrt{\frac{8a^\circ w}{\pi \mathcal{E}}}. \tag{2.19}$$

Equivalently, the stationary point (a°, h°) is a root of the function

$$(a, h) \mapsto \chi(a; h) + \sqrt{\frac{8aw}{\pi \mathcal{E}}}. \tag{2.20}$$

It follows from (2.11) and (2.20) and the *implicit function theorem* that there exists a function $\hbar$ that is defined on a neighborhood of a° such that

$$h^\circ = \hbar(a^\circ). \tag{2.21}$$

We derive $\hbar$ for contact experiments involving a spherical and conical tip in Sections 3.1 and 3.2, respectively.

First order necessary condition. It can be shown that $\Pi(\cdot, \cdot; \Delta)$ is continuously differentiable on $\text{int}(\mathcal{D})$. Consequently, if (a^*, h^*) is an interior solution point, then it must also be a stationary point. Therefore, an interior solution point (a^*, h^*) is also a root of the function (2.20) and it satisfies the equation $h^* = \hbar(a^*)$.

Second order necessary condition. We discuss the second order conditions in Appendix C. A consequence of those conditions is that the value of the function $g : [0, \infty) \to \mathbb{R}$, where

$$g(a) := \hbar'(a) - \frac{\sqrt{8\pi a \mathcal{E} w}}{2a\mathcal{E} + k_s} \tag{2.22}$$

at an interior solution point's abscissa should be non-negative. The derivative of $\hbar$ is denoted as $\hbar'$.

Second order sufficient condition. We show in C.3.1 that a stationary point (a°, h°) is a solution point if

$$g(a^\circ) > 0. \tag{2.23}$$

Eq. (2.23) is the second order sufficiency condition (C.12) written in terms of the function g, which we introduced in (2.22).

2.3.2. Contact force

In our contact problem, the contact force between the tip and the substrate can be written as $P\hat{\mathbf{e}}_z$. When P in non-negative (resp. non-positive), we say that the contact force is compressive (resp. attractive). The contact force corresponding to the solution point (a^*, h^*) is denoted as P^*.

As we discussed in Section 2.3.1, the solution points (a^*, h^*) belonging to $\partial\mathcal{D}$ are of the form $(0, \Delta)$, where $\Delta < 0$. In the solutions corresponding to those points, the spring is unstretched, the substrate is undeformed, and the tip and the substrate are not in physical contact. (See Appendix A for details.) Therefore, the contact force $P^* = 0$ in those solutions.

When (a^*, h^*) belongs to the $\text{int}(\mathcal{D})$ it follows from the results presented by Sneddon (1965) and Kesari and Lew (2012, 5.10) that the contact force P^* is

$$P^* = \mathcal{P}(a^*, h^*), \tag{2.24a}$$

where $\mathcal{P} : \mathcal{D} \to \mathbb{R}$

and

$$\mathcal{P}(a, h) := \pi \mathcal{E} \int_0^a \chi(r; h)\, dr. \tag{2.24b}$$

As we discussed in Section 2.3.1, by necessity an interior solution point is also a stationary point. Thus, we can replace a° and h° with, respectively, a^* and h^* in (2.18) and (2.19), and then, from (2.24), substitute $\pi \mathcal{E} \int_0^{a^*} \chi(\tilde{a}; h^*)\, d\tilde{a}$ with P^* in the first of the resulting equations to get

$$\Delta = \frac{P^*}{k_s} + h^* \tag{2.25}$$

and

$$\chi(a^*; h^*) = -\sqrt{\frac{8a^* w}{\pi \mathcal{E}}}. \tag{2.26}$$

We determine the solution contact radius, indentation depth, and contact force, i.e., a^*, h^*, and P^*, through simultaneously solving the Eqs. (2.24a)–(2.26). We illustrate this in Sections 3.1 and 3.2, respectively, where we consider tips having spherical and conical shapes.

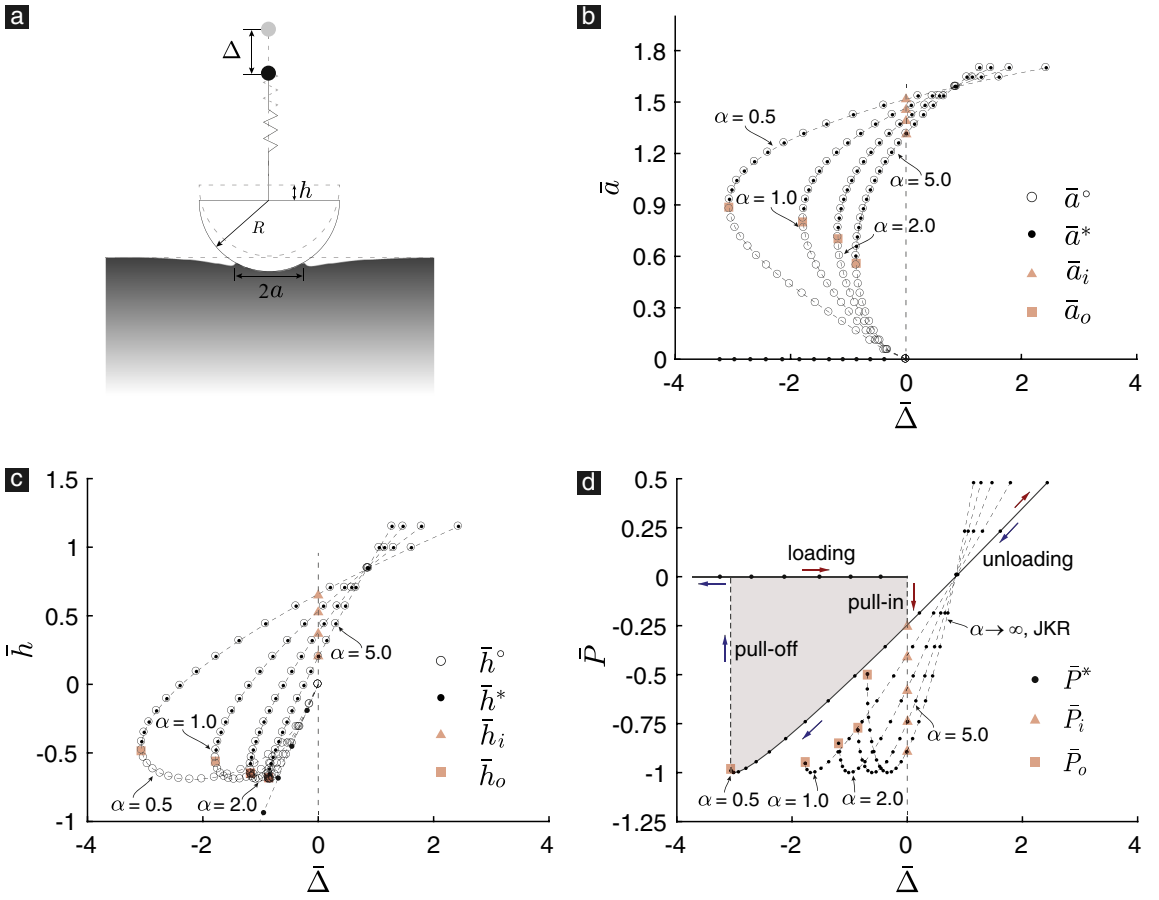

Fig. 4. (a) Geometry of the spherical-tip contact problem. In (b)–(d) we denote the different tip-substrate configurations as points. A configuration's abscissa gives its prescribed state displacement $\bar{\Delta}$. In (b) and (c) the ordinate of each configuration gives its contact radius and indentation depth, respectively. The configurations whose contact radii and indentation depths corresponding to stationary points are marked as circles, while those corresponding to solution points are marked as dots. In (d) the ordinate of a configuration gives its contact force $\bar{P}^*$. The configurations just after the occurrence of the pull-in instability are marked by triangles, while the configurations just before the occurrence of the pull-off instability are marked by squares.

3. Applications

3.1. Spherical tip

3.1.1. Theory

In AFM-type contact experiments involving a substrate that is especially delicate, such as a gel or a biological tissue, it is customary to use a spherical glass or polystyrene bead as the tip (Bouchonville et al., 2016; Kesari et al., 2010; Notbohm et al., 2012; Sun et al., 2004). The radial profile of the spherical tip can be written as

$$f(r) = R(1 - r^2/R^2)^{1/2},$$

where $0 \le r < R$ and R is the sphere's radius, see Fig. 4a. For this particular f on calculating $\tilde{u}_z$ from (2.1) and substituting it into (2.11), we get

$$\chi(\tilde{a}; h) = \frac{2}{\pi}\left[h - \tilde{a}\tanh^{-1}\left(\frac{\tilde{a}}{R}\right)\right]. \tag{3.1}$$

From (3.1), it follows that in the limit $\tilde{a}/R \to 0$

$$\frac{\chi(\tilde{a}; h)}{R} = \frac{2}{\pi}\left[\frac{h}{R} - \left(\frac{\tilde{a}}{R}\right)^2\right] + O\left(\frac{\tilde{a}^4}{R^4}\right). \tag{3.2}$$

Generally, when measuring compliant materials, the contact radius must be made large enough that the contact force is measurable. Because of this, during some stages of the experiments the contact radius a is not substantially smaller than

the bead radius R. Despite that, in order to simplify some of the ensuing calculations in this section, we assume that the contact radius during the experiment is much smaller than R. That is, we ignore the fourth order term in (3.2) and simply take

$$\chi(\tilde{a}; h) = \frac{2}{\pi}\left(h - \frac{\tilde{a}^2}{R}\right). \tag{3.3}$$

Substituting (3.3) in (2.18) and (2.19), we find that the points (a°, h°) satisfy the equations

$$h^\circ = \hbar(a^\circ), \tag{3.4a}$$

where

$$\hbar(a^\circ) = \frac{a^{\circ 2}}{R} - \sqrt{\frac{2\pi a^\circ w}{\mathcal{E}}} \tag{3.4b}$$

and

$$\Delta = \frac{\mathcal{P}(a^\circ, h^\circ)}{k_s} + h^\circ, \tag{3.5a}$$

where

$$\mathcal{P}(a^\circ, h^\circ) = 2a^\circ h^\circ \mathcal{E} - \frac{2a^{\circ 3}\mathcal{E}}{3R}. \tag{3.5b}$$

Recall from Section 2.3 that a stationary point (a°, h°) is a solution point if it satisfies the condition (2.23). We can compute the derivative of the function $\hbar$ given in (3.4b) and substitute it into (2.22) to determine the function g, and then substitute g in (2.23). In doing this, we find that (a°, h°) is a solution point if

$$g(a^\circ) = \frac{2a^\circ}{R} - \sqrt{\frac{\pi w}{2a^\circ \mathcal{E}}} - \frac{\sqrt{8\pi a^\circ \mathcal{E} w}}{2a^\circ \mathcal{E} + k_s} \tag{3.6}$$

is positive.

The non-dimensional variables and parameters $\bar{\mathcal{P}}(\bar{a}^\circ, \bar{h}^\circ) := \mathcal{P}(a^\circ, h^\circ)/\hat{P}$, $\bar{\hbar}(\bar{a}^\circ) := \hbar(a^\circ)/\hat{h}$, and $\bar{\Delta} = \Delta/\hat{h}$, where $\bar{a}^\circ = a^\circ/\hat{a}$, $\bar{h}^\circ = h^\circ/\hat{h}$, $\hat{P} := 3\pi wR/2$, $\hat{a} := \left(9\pi wR^2/8\mathcal{E}\right)^{1/3}$, and $\hat{h} := (\hat{a}^2/R)$ allow Eqs. (3.4) and (3.5) to be written as, respectively,

$$\bar{h}^\circ = \bar{\hbar}(\bar{a}^\circ), \tag{3.7a}$$

where

$$\bar{\hbar}(\bar{a}^\circ) = \bar{a}^{\circ 2} - \frac{4}{3}\bar{a}^{\circ 1/2} \tag{3.7b}$$

and

$$\bar{\Delta} = \frac{4}{3\alpha}\bar{\mathcal{P}}\left(\bar{a}^\circ, \bar{h}^\circ\right) + \bar{h}^\circ, \tag{3.8a}$$

where

$$\bar{\mathcal{P}}\left(\bar{a}^\circ, \bar{h}^\circ\right) = \frac{3}{2}\bar{a}^\circ \bar{h}^\circ - \frac{1}{2}\bar{a}^{\circ 3}. \tag{3.8b}$$

Defining $\bar{g}(\bar{a}^\circ) := \bar{a}^{\circ 1/2} g(\bar{a}^\circ \hat{a})/(3\pi w/(8\mathcal{E}R))^{1/3}$ and with the non-dimensional parameters $\hat{a}$ and α, we get from (3.6) that

$$\bar{g}(\bar{a}^\circ) = 3\bar{a}^{\circ 3/2} - \frac{4\bar{a}^\circ}{2\bar{a}^\circ + \alpha} - 1. \tag{3.9}$$

The parameter α in (3.8a) and (3.9) is the ratio of the machine stiffness k_s to the contact interface's characteristic stiffness $\hat{k}_s := \left(9\pi w\mathcal{E}^2R^2/8\right)^{1/3}$.

3.1.2. Numerical calculation of pull-in and pull-off forces and hysteretic energy loss

We numerically computed the stationary points for a range of $\bar{\Delta}$ values using (3.7) and (3.8). The results from these calculations are shown in Fig. 4b and c. It follows from the discussion in Appendix A that the pull-in instability occurs when $\bar{\Delta} = 0$. The contact radius just after the pull-in instability, $\bar{a}_i$, is the abscissa of the stationary point that satisfies (3.7) and (3.8) for $\bar{\Delta}$=0. We define the pull-off contact radius $\bar{a}_o$ to be $\arg\inf\{\bar{a}^\circ \mid \bar{g}(\bar{a}^\circ) > 0\}$. The indentation-depths just prior to the pull-in instability and pull-off instability are, respectively, $\bar{h}_i = \bar{\hbar}(\bar{a}_i)$ and $\bar{h}_o = \bar{\hbar}(\bar{a}_o)$, where $\bar{\hbar}$ for the spherical tip is given in (3.7b). We marked $\bar{a}_i$ and $\bar{a}_o$ in Fig. 4b, and $\bar{h}_i$ and $\bar{h}_o$ in Fig. 4c.

We define a non-dimensional solution point to be $(\bar{a}^*, \bar{h}^*) := (a^*/\hat{a}, h^*/\hat{h})$. A stationary point $(\bar{a}^\circ, \bar{h}^\circ)$ qualifies as a non-dimensional solution point if its abscissa satisfies the sufficiency condition that $\bar{g}(\bar{a}^\circ)$ in (3.9) is positive. We show the abscissa and ordinate of several of these solution points in Fig. 4a and b, respectively, using solid symbols. In addition to the solution points that we have from the set of stationary points, it follows from the discussion of Section 2.3.1 that when

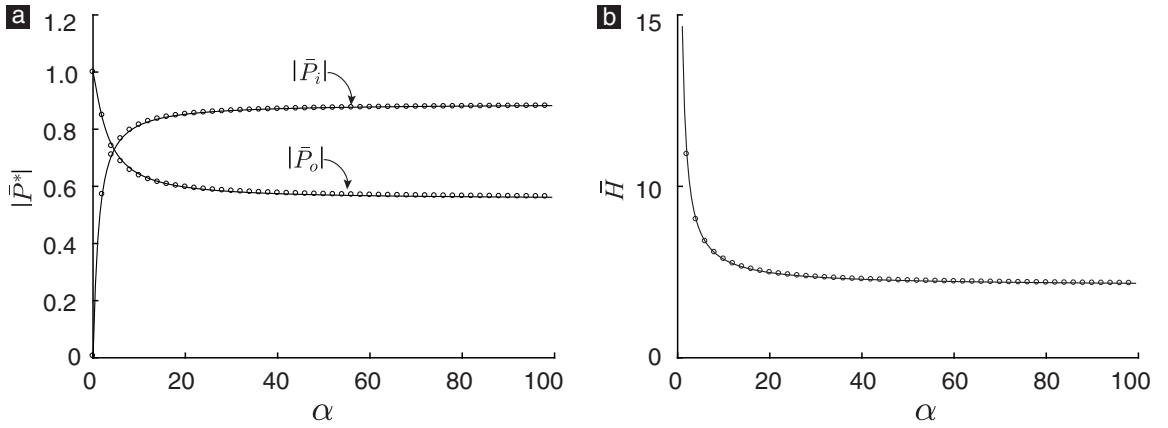

Fig. 5. The spherical-tip case. (a) The exact (circles) and approximate (solid line) values of $|\bar{P}_i|$ and $|\bar{P}_o|$ as a function of α. The exact values are computed using the procedure outlined in Section 3.1.2. The approximate values are given by the functions $\bar{\mathcal{P}}_i$ and $\bar{\mathcal{P}}_o$ defined in (3.10). (b) The exact (circles) and approximate (solid line) values of $\bar{H}$ as a function of α. The exact values are computed using (3.11), while the approximate values are given by the function $\bar{\mathcal{H}}$ defined in (3.12).

$\bar{\Delta} < 0$ we have additional solution points on the boundary $\partial\mathcal{D}$ that are of the form $(0, \bar{\Delta})$. The abscissa and ordinate of these points are also marked in Fig. 4b and c, respectively.

For each of the solution points $(\bar{a}^*, \bar{h}^*)$ shown in Fig. 4b and c, we computed the non-dimensional contact force $\bar{P}^* := P^*/\hat{P}$ as $\bar{\mathcal{P}}(\bar{a}^*, \bar{h}^*)$, where $\bar{\mathcal{P}}$ for the spherical tip is given in (3.8b). We show these force values in Fig. 4d. The contact forces corresponding to the solution points of the form $(0, \bar{\Delta})$, which are actually all zero, are also shown in that figure.

We denote the contact force and the stage displacement just prior to the occurrence of the pull-in (resp. pull-off) instability as $\bar{P}_i^*$ (resp. $\bar{P}_o^*$) and $\bar{\Delta}_i$ (resp. $\bar{\Delta}_o$). Recall that $\bar{\Delta}_i = 0$. It follows from (3.8a) that

$$\bar{\Delta}_o = \frac{4}{3\alpha}\bar{\mathcal{P}}(\bar{a}_o, \bar{h}_o) + \bar{h}_o.$$

The pull-in and pull-off contact forces, i.e., $\bar{P}_i^*$ and $\bar{P}_o^*$, can be calculated as $\bar{\mathcal{P}}(\bar{a}_i, \bar{h}_i)$ and $\bar{\mathcal{P}}(\bar{a}_o, \bar{h}_o)$, respectively, where $\bar{\mathcal{P}}$ for the spherical tip is given in (3.8b). We have marked the points $(\bar{\Delta}_i, \bar{P}_i^*)$ and $(\bar{\Delta}_o, \bar{P}_o^*)$ in Fig. 4d.

We show the contact forces $\bar{P}_i^*$ and $\bar{P}_o^*$ as a function of α in Fig. 5a. Through an analysis of (3.7) and (3.8), we found that as $\alpha \to 0$ the contact forces $\bar{P}_i^*$ and $\bar{P}_o^*$ tend to 0 and -1, respectively. And as $\alpha \to \infty$, the contact forces $\bar{P}_i^*$ and $\bar{P}_o^*$ tend to $-8/9$ and $-5/9$, respectively. With the aid of these asymptotic results we were able to construct the functions $\bar{\mathcal{P}}_i^*$, $\bar{\mathcal{P}}_o^* : (0, \infty) \to (-\infty, 0)$, where

$$\bar{\mathcal{P}}_i^*(\alpha) = -\frac{8}{9}\left(1 - \frac{1}{1 + 0.83\alpha^{1.12}}\right) \tag{3.10a}$$

and

$$\bar{\mathcal{P}}_o^*(\alpha) = -\frac{1}{9}\left(5 + \frac{4}{1 + 0.21\alpha^{1.32}}\right). \tag{3.10b}$$

These provide excellent approximations for $\bar{P}_i^*$ and $\bar{P}_o^*$ for a wide range of α values. (See Fig. 5a.)

As can be noted from Fig. 4b and c, there exist two solution points for some $\bar{\Delta}$ values. For those same values, unsurprisingly, there are also two force values. Which of these two force values are actually measured in an experiment depends on the contact cycle employed in that experiment. For example, for the typical contact cycle discussed in Section 1, the experiment will measure the force values that we have marked using right and left arrows in Fig. 4d during the loading and the unloading phases, respectively.

The hysteretic energy loss during a contact cycle can be computed as $(R^4 w^5/\mathcal{E}^2)^{1/3}\bar{H}$, where

$$\bar{H} = \frac{4}{3\alpha}\int_{\bar{a}_o}^{\bar{a}_i} \bar{\mathcal{P}}(\bar{a}^*, \bar{h}(\bar{a}^*))\left[\bar{\mathcal{P}}_{,1}(\bar{a}^*, \bar{h}(\bar{a}^*)) + \bar{\mathcal{P}}_{,2}(\bar{a}^*, \bar{h}(\bar{a}^*))\bar{h}'(\bar{a}^*) + \frac{3\alpha}{4}\bar{h}'(\bar{a}^*)\right] d\bar{a}^*, \tag{3.11}$$

in which $\bar{\mathcal{P}}_{,1}$ and $\bar{\mathcal{P}}_{,2}$ are the partial derivatives of $\bar{\mathcal{P}}$ with respect to its first and second arguments, respectively. It can be shown that as $\alpha \to 0$ the hysteretic energy loss $\bar{H} \to \infty$, and as $\alpha \to \infty$ the hysteretic energy loss $\bar{H} \to (\pi^{5/3} + 3(2\pi)^{5/3})/10\ (\approx 7.092)$. With the aid of these asymptotic results, we constructed the function $\bar{\mathcal{H}} : (0, \infty) \to (0, \infty)$, where

$$\bar{\mathcal{H}}(\alpha) = 7.092 + \frac{7.657}{\alpha^{0.99}}. \tag{3.12}$$

The values of $\bar{\mathcal{H}}$ are very close to $\bar{H}$ for a wide range of α values, see Fig. 5b.

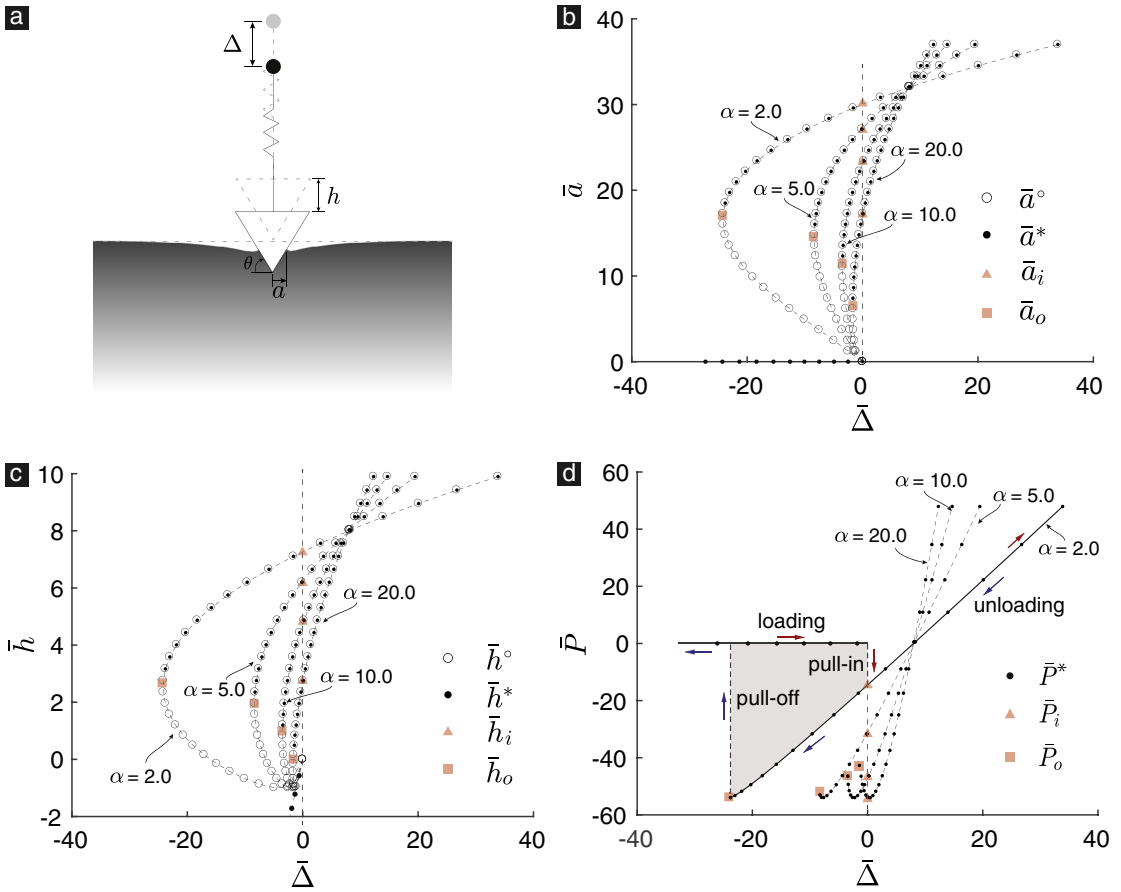

Fig. 6. (a) Geometry of the conical-tip contact problem. In (b)–(d) we denote the different tip-substrate configurations as points. A configuration's abscissa gives its prescribed state displacement $\bar{\Delta}$. In (b) and (c) the ordinate of each configuration gives its contact radius and indentation depth. The configurations whose contact radii and indentation depths corresponding to stationary points are marked as circles, while those that corresponding to solution points are marked as dots. In (d) the ordinate of a configuration gives its contact force $\bar{P}^*$. The configurations just after the occurrence of the pull-in instability are marked by triangles, while the configurations just before the occurrence of the pull-off instability are marked by squares.

3.2. Conical tip

3.2.1. Theory

In this section, we consider a conical tip whose radial profile $f(r) = -r\tan\theta$, where $\theta \in (0, \pi/2)$ is shown marked in Fig. 6a. Calculating $\tilde{u}_z$ from (2.1) for this radial profile and substituting it into (2.11) results in

$$\chi(\tilde{a}; h) = \frac{2}{\pi}\left(h - \frac{\pi}{2}\tilde{a}\tan\theta\right). \tag{3.13}$$

As we did in the case of the spherical tip (Section 3.1), by substituting (3.13) in (2.18) and (2.19) we obtain that the points (a°, h°) satisfy the equations

$$h^\circ = \hbar(a^\circ), \tag{3.14a}$$

where

$$\hbar(a^\circ) = 2a^\circ h^\circ \mathcal{E} - \frac{1}{2}\pi a^{\circ 2}\mathcal{E}\tan\theta \tag{3.14b}$$

and

$$\Delta = \frac{\mathcal{P}(a^\circ, h^\circ)}{k_s} + h^\circ, \tag{3.15a}$$

where

$$\mathcal{P}(a^\circ, h^\circ) = 2a^\circ h^\circ \mathcal{E} - \frac{1}{2}\pi a^{\circ 2}\mathcal{E}\tan\theta. \tag{3.15b}$$

From (2.22) and (3.14b), it follows that the function g for the case of conical tip is

$$g(a^\circ) = \frac{\pi}{2}\tan\theta - \sqrt{\frac{\pi w}{2a^\circ \mathcal{E}}} - \frac{\sqrt{8\pi a^\circ \mathcal{E} w}}{2a^\circ \mathcal{E} + k_s}. \tag{3.16}$$

The functions with non-dimensional values and non-dimensional variables $\bar{\mathcal{P}}(\bar{a}^\circ, \bar{h}^\circ) := \mathcal{P}(a^\circ, h^\circ)/\hat{P}$, $\bar{h}(\bar{a}^\circ) := h(a^\circ)/\hat{h}$, and $\bar{\Delta} := \Delta/\hat{h}$, where $\bar{a}^\circ := a^\circ/\hat{a}$, $\bar{h}^\circ := h^\circ/\hat{h}$, $\hat{P} := w^2/(\pi \mathcal{E}\tan^3\theta)$, $\hat{a} := w/(\pi \mathcal{E}\tan^2\theta)$, and $\hat{h} := w/(\mathcal{E}\tan\theta)$, allow (3.14) and (3.15) to be written as, respectively,

$$\bar{h}^\circ = \bar{h}(\bar{a}^\circ), \tag{3.17a}$$

where

$$\bar{h}(\bar{a}^\circ) = \frac{\bar{a}^\circ}{2} - (2\bar{a}^\circ)^{1/2} \tag{3.17b}$$

and

$$\bar{\Delta} = \frac{1}{\alpha}\bar{\mathcal{P}}\left(\bar{a}^\circ, \bar{h}^\circ\right) + \bar{h}^\circ, \tag{3.18a}$$

where

$$\bar{\mathcal{P}}\left(\bar{a}^\circ, \bar{h}^\circ\right) = 2\bar{a}^\circ \bar{h}^\circ - \frac{1}{2}\bar{a}^{\circ 2}. \tag{3.18b}$$

The parameter α in (3.18a) is the ratio of the machine stiffness k_s to the contact interface's characteristic stiffness $\hat{k}_s := w/(\pi\tan^2\theta)$. Defining $\bar{g}(\bar{a}^\circ) := (2\bar{a}^\circ)^{1/2} g(\bar{a}^\circ \hat{a})/(\pi\tan\theta)$, we find from (3.16) and the definitions of α and $\hat{a}$ that

$$\bar{g}(\bar{a}^\circ) = \frac{\sqrt{2\bar{a}^\circ}}{2} - \frac{4\bar{a}^\circ}{2\bar{a}^\circ + \alpha} - 1. \tag{3.19}$$

3.2.2. Numerical calculation of the pull-in and pull-off forces and the hysteretic energy loss

We numerically computed the stationary points $(\bar{a}^\circ, \bar{h}^\circ)$ for a range of $\bar{\Delta}$ values using (3.17) amd (3.18). The solution points $(\bar{a}^*, \bar{h}^*)$ are those stationary points $(\bar{a}^\circ, \bar{h}^\circ)$ for which $\bar{g}(\bar{a}^\circ) > 0$, with $\bar{g}$ being given in (3.19). When $\bar{a}^* > 0$ then $\bar{P}^* = \bar{\mathcal{P}}(\bar{a}^*, \bar{h}^*)$, where $\bar{\mathcal{P}}$ is given in (3.18b). When $\bar{a}^* = 0$, then $P^* = 0$. We show the abscissa (resp. ordinate) of the stationary and solution points as a function of $\bar{\Delta}$ in Fig. 6b (resp. c), and show $\bar{P}^*$ in Fig. 6d.

We employed the same procedure that we used in Section 3.1 to identify the contact radii $\bar{a}_i$ and $\bar{a}_o$, indentation depths $\bar{h}_i$ and $\bar{h}_o$, and contact forces $\bar{P}_i$ and $\bar{P}_o$ to identify those quantities in the case of conical tip (Fig. 6b–d). We found that as $\alpha \to 0$ the contact forces $\bar{P}_i^*$ and $\bar{P}_o^*$ approach 0 and -54, respectively. And as $\alpha \to \infty$, the contact forces $\bar{P}_i^*$ and $\bar{P}_o^*$ approach -32 and -6, respectively. With the aid of these asymptotic results, we were able to construct the functions $\bar{\mathcal{P}}_i^*$ and $\bar{\mathcal{P}}_o^*$: $(0,\infty) \to (-\infty, 0)$, where

$$\bar{\mathcal{P}}_i^*(\alpha) = -32\left(1 - e^{-0.12\alpha}\right)\left(1 + 2.05e^{-0.123\alpha^{0.665}}\right) \tag{3.20a}$$

and

$$\bar{\mathcal{P}}_o^*(\alpha) = -6 - \frac{48}{1 + 0.00158\alpha^{2.285}} \tag{3.20b}$$

whose values approximate, respectively, $\bar{P}_i^*$ and $\bar{P}_o^*$ very closely for a wide range of α (Fig. 7a).

We computed the hysteretic energy loss during a contact cycle as $w^3\bar{H}/(\pi\mathcal{E}^2\tan^4\theta)$, where

$$\bar{H} = \frac{1}{\alpha}\int_{\bar{a}_o}^{\bar{a}_i} \bar{\mathcal{P}}(\bar{a}^*, \bar{h}(\bar{a}^*))\left[\bar{\mathcal{P}}_{,1}(\bar{a}^*, \bar{h}(\bar{a}^*)) + \bar{\mathcal{P}}_{,2}(\bar{a}^*, \bar{h}(\bar{a}^*))\bar{h}'(\bar{a}^*) + \alpha\bar{h}'(\bar{a}^*)\right] d\bar{a}^*, \tag{3.21}$$

in which $\bar{h}$ and $\bar{\mathcal{P}}$ are given in (3.17b) and (3.18b), respectively. We found that as $\alpha \to 0$ the hysteretic energy loss $\bar{H} \to \infty$, and as $\alpha \to \infty$ the hysteretic energy loss $\bar{H} \to 22$. With the aid of these asymptotic results we were able to construct the function $\bar{\mathcal{H}}$: $(0,\infty) \to (0,\infty)$, where

$$\bar{\mathcal{H}}(\alpha) = 22 + \frac{4383.87}{\alpha^{1.4478}}, \tag{3.22}$$

whose value is very close to $\bar{H}$ for a wide range of α (Fig. 7b).

4. Experimental comparison and discussion

4.1. Experimental comparison

In this section, we compare our model to the experiments reported by Sun et al. (2004) and Notbohm et al. (2012). Both experiments involved adhesive elastic contact between a PDMS slab and an AFM tip. The AFM tip in Sun *et al.*'s experiments was a Si_3N_4 bead of radius $R = 58$ nm. In Notbohm et al. experiments the AFM tip was a glass bead with $R = 2.5$ μm.

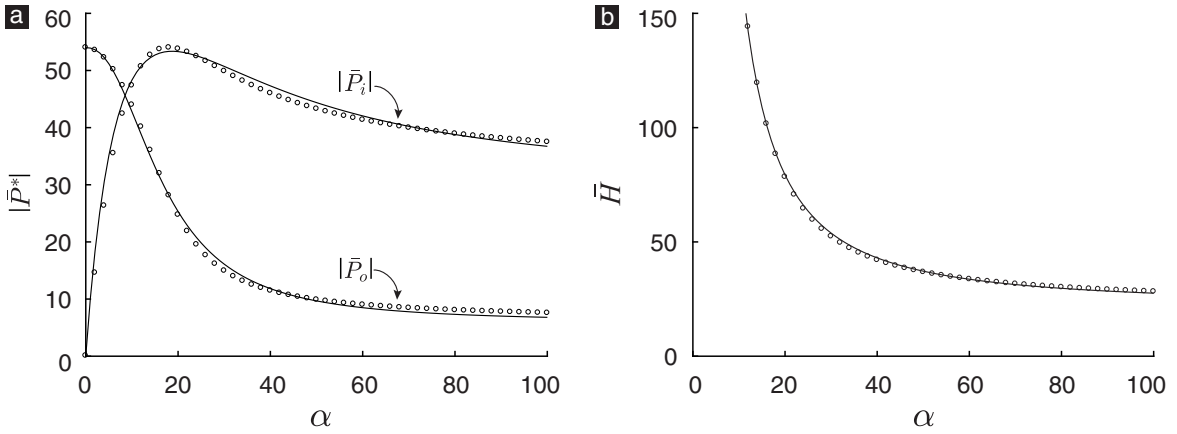

Fig. 7. The conical-tip case. (a) The exact (circles) and approximate (solid line) values of $|\bar{P}_i|$ and $|\bar{P}_o|$ as a function of α. The exact values are computed using the procedure outlined in Section 3.2.2. The approximate values are given by the functions $\bar{\mathcal{P}}_i$ and $\bar{\mathcal{P}}_o$ defined in (3.20). (b) The exact (circles) and approximate (solid line) values of $\bar{H}$ as a function of α. The exact values are computed using (3.21), while the approximate values are given by the function $\bar{\mathcal{H}}$ defined in (3.22).

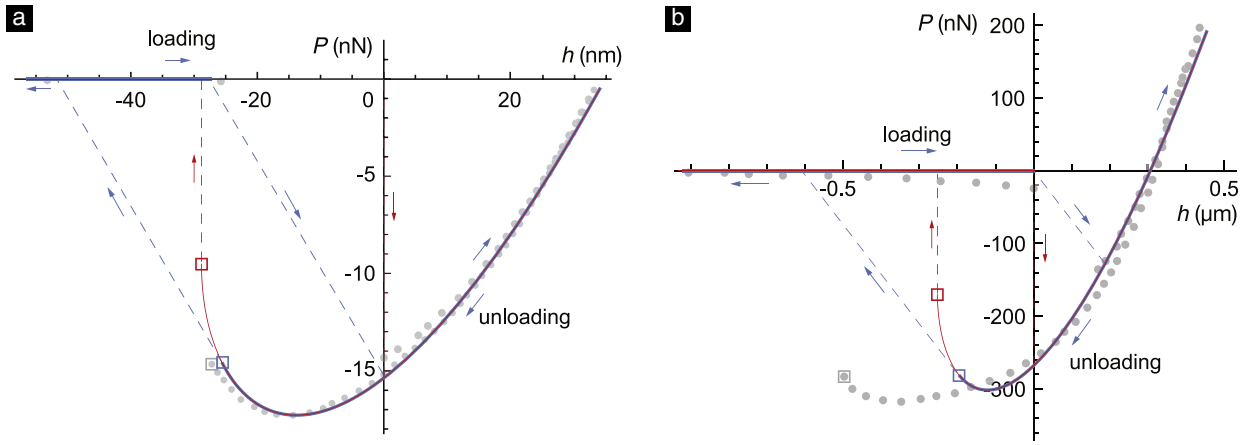

Fig. 8. Comparison of the contact force–indentation depth curves predicted by our (blue lines) and the JKR (red lines) models with experimental data (gray dots). The data in (a) and (b) are, respectively, from the experiments performed by Sun et al. (2004) and Notbohm et al. (2012). In each of the curves and data sets, the configuration just before the occurrence of the pull-off instability is marked with a square. (For interpretation of the references to color in this figure legend, the reader is referred to the web version of this article.)

In Fig. 8a we show the contact force–indentation depth data from a representative contact cycle in Sun et al. experiments as gray dots. In that same figure, we show the best fit of our model, specifically (3.4b) and (3.5b), as blue curves and the JKR model as red curves. For both models, we use $\mathcal{E}$ and w as the fitting parameters. (See Appendix D for details.) These parameters come out to be 6.39 MPa and 63.2 mJ/m^2, respectively, in the best fit of both our model and the JKR model. Sun et al. (2004) report the stiffness of the AFM cantilever in their experiments to be $k_s = 0.66$ N/m. Using this value, the best fit of our model predicts the pull-off force to be -14.73 nN, whereas the best fit of the JKR model predicts it to be -5 $-5\pi wR/6 = -9.59$ nN. As can be seen in Fig. 8a, the experimental pull-off force is -14.8 nN. Thus, the prediction of the pull-off force from our model is much closer to the experimental value than the prediction of the JKR model.

An important experimental feature that is uniquely captured by our model is that in the experiments, the indentation depth changes by a finite amount during the pull-in and pull-off instabilities. For example, in the data shown in Fig. 8a, the indentation depth changes by 26.7 nm and 26.9 nm during the pull-in and pull-off instabilities, respectively. In alignment with these observations, the best fit of our model predicts the indentation depth during the instabilities to change by 27.4 nm and 26 nm, respectively. In distinct contrast, the JKR model always predicts there to be no change in the indentation depth during either of the instabilities.

Fig. 8b shows the contact force–indentation depth data from a representative contact cycle in Notbohm et al. experiments as gray dots. The best fits of our model and the JKR model are shown in Fig. 8b as blue and red curves, respectively. In the best fits of both our model and the JKR model, $\mathcal{E}$ and w come out to be 0.65 MPa and 25.7 J/m^2, respectively. The AFM cantilever's stiffness in Notbohm et al. experiments was $k_s = 0.642$ N/m. Using this value for the machine stiffness, we find the pull-off contact force in the best fit of our model to be -281.5 nN. This value is remarkably close to the

experimental pull-off force value, which is −281.6 nN. In contrast, the pull-off force in the best fit of the JKR theory is $-5\pi wR/6 = -167.5$ nN, which is significantly greater than the experimental value. The changes in the indentation depth during the occurrence of the pull-in and pull-off instabilities in the experiments are 0.17 μm and 0.41 μm, respectively. These changes in the best fit of our model are, respectively, 0.19 μm and 0.42 μm, which are very close to the experimental values.

4.2. Discussion

There is a significant discrepancy between the best fits of our model, the JKR model, and the experiments towards the end of the unloading phase. (See Fig. 8b.) Notbohm et al. (2012) argue that the discrepancy between their data and the JKR model towards the end of the unloading phase was due to the nonlinear deformation behavior of the AFM cantilever. However, we believe that this discrepancy requires further investigation.

There is also a discrepancy between the best fits of our model, the JKR model, and Notbohm et al. experimental data just prior to the occurrence of the pull-in instability. Prior to the occurrence of the pull-in instability, there is no contact force in either our model or the JKR model. However, as can be noted in Fig. 8b, in Notbohm et al. experiments there are some small, but non-negligible, negative contact forces prior to the occurrence of the pull-in instability. We believe that this discrepancy is due to the assumption in our model that the interbody adhesive interactions are infinitesimally short ranged. As we discussed in Section 1, dry adhesion mostly originates from van der Waals and Coulombic type interactions, which have a finite interaction range. The finite ranged interactions can give rise to negative forces between the tip and the substrate even prior to the occurrence of the pull-in instability. This view is supported by molecular statics simulations of adhesive elastic contact (Deng and Kesari, 2017), in which the interbody interactions are taken to have a finite range and the contact forces in them are seen to be non-zero prior to the occurrence of the pull-in instability.

A further implication of our assumption that the interbody adhesive interactions are infinitesimally short ranged is that our model's prediction that the pull-in instability occurs when $\Delta = 0$ is also quite likely to be inconsistent with experiments. In experiments, the pull-in instability is likely to occur when $\Delta < 0$, although it might be difficult to experimentally demonstrate this fact since identifying the datum of Δ is quite challenging in adhesive elastic contact experiments.

Acknowledgments

This work was supported by the National Science Foundation through the Mechanics of Materials and Structures Program award number 1562656. Weilin Deng is partially supported by a graduate fellowship from the China Scholarship Council.

Appendix A. Solutions on the boundary of the domain $\mathcal{D}$

In this section we study the solutions as defined by (2.14) that lie on the boundary of the domain $\mathcal{D}$ of the function $\Pi(\cdot, \cdot; \Delta)$. Recall that the domain of $\Pi(\cdot, \cdot; \Delta)$ is the set $\mathcal{D} := \{(a, h) \in \mathbb{R}^2 : a \geq 0\}$. Therefore, the domain boundary $\partial\mathcal{D}$ is simply the set of points in $\mathbb{R}^2$ that are of the form $(0, h)$. As we will show, the solution points on $\partial\mathcal{D}$ could only exist in the form of $(0, \Delta)$ when $\Delta < 0$. At these points, there is no deformation of the elastic spring and the tip and the substrate are not in physical contact.

A1. Points of the form (0, h) where h > 0 cannot be solutions

A point of the form $(0, h)$ where $h > 0$ cannot be a solution to our contact mechanics problem. Given any $\delta > 0$, the neighborhood $B(0, h, \delta)$ of $(0, h)$ contains the point $(\delta/2, h)$. The value of $\Pi(\cdot, \cdot; \Delta)$ at $(\delta/2, h)$, as given by the first line in (2.12), is finite and smaller than its value at $(0, h)$. As can be determined by the third line of (2.12), it is also unbounded. That is, we are always able to find a point in the neighborhood of $(0, h)$, no matter how small the neighborhood's diameter, where the value of $\Pi(\cdot, \cdot; \Delta)$ is smaller than at $(0, h)$. Consequently, the point $(0, h)$ cannot be a solution.

A2. A point (a, h) where a = 0 and h < 0 is a solution iff Δ < 0 and h = Δ

The difference in the value of $\Pi(\cdot, \cdot; \Delta)$ at a point $(0, h)$, where $h < 0$, and a neighboring point $(\delta a, h + \delta h)$, where $\delta a \geq 0$, can be expressed as

$$\Pi[\delta a, h + \delta h; \Delta] - \Pi[0, h; \Delta] = \mathcal{E}h^2\delta a + k_s\delta h(h - \Delta) + O(\|(\delta a, \delta h)\|^2) \tag{A.1}$$

in the limit of $(\delta a, \delta h) \to (0, 0)$. Any sequence of points converging to $(0, h)$ where $h < 0$ can be expressed as $(\delta a_n, h + \delta h_n)_{n\in\mathbb{N}}$, where $\delta a_n \geq 0$ and the sequence $(\delta a_n, \delta h_n)$ converges to (0,0). Consider the case $\Delta < 0$ and $h = \Delta$. It follows from (A.1) that there exists an $N \in \mathbb{N}$ such that for all $n > N$ the sign of the difference $\Pi[a_n, h_n; \Delta] - \Pi[0, h; \Delta]$ is the same as that of the leading order term $\mathcal{E}h^2\delta a_n$. Because both $\mathcal{E}$ and δa_n are positive, the leading order term is positive. This result implies that when $\Delta < 0$, the point $(0, \Delta)$ is always a solution.

Now consider the case $h \neq \Delta$ and the sequence of points $(a_n, h_n)_{n\in\mathbb{N}}$ where $a_n = 0$ and $h_n = h - (h - \Delta)/n$. This sequence of points also converge to $(0, h)$. It follows from (A.1) that there exists an $N \in \mathbb{N}$ such that for all $n > N$ the sign of the difference $\Pi[a_n, h_n; \Delta] - \Pi[0, h; \Delta]$ is the as same that of the term $-k_s(h - \Delta)^2/n$, which is negative because $k_s > 0$. Therefore,

when $h \neq \Delta$, the point $(0, h)$ where $h < 0$ cannot be a solution. Therefore, it is implied that that a point of the form $(0, h)$ where $h < 0$ is a solution iff $\Delta < 0$ and $h = \Delta$.

A3. The point $(a, h) = (0, 0)$ cannot be a solution

In this section we show that the point $(a, h) = (0, 0)$ cannot be a solution at any given Δ. We demonstrate this by showing that no matter how small δ is, there will always exist points in $B(0, 0, \delta)$ where the value of $\Pi(\cdot, \cdot; \Delta)$ is smaller than its value at $(a, h) = (0, 0)$. We begin by deriving an asymptotic series expansion for $\Pi(\cdot, \cdot; \Delta)$ in the limit $(a, h) \to 0$, with $a > 0$. In the limit $\tilde{a} \to 0$ we know from (2.1) and (2.11) that

$$\chi(\tilde{a}; h) = \frac{2h}{\pi} + \tilde{a} f'(0) + \frac{2\tilde{a}^2}{\pi} f''(0) + O(\tilde{a}^3), \tag{A.2}$$

where O is the Bachmann–Landau "Big-Oh" symbol. We then obtain

$$\chi(\tilde{a}; h)^2 = \frac{4h^2}{\pi^2} + \frac{4ahf'(0)}{\pi} + a^2\left(\frac{8\ hf''(0)}{\pi^2} + f'(0)^2\right) + O(\tilde{a}^3). \tag{A.3}$$

After substituting (A.3) into (2.12) and simplifying, we determine that

$$\begin{aligned}\frac{\pi^2 \mathcal{E}}{4}\int_0^a \chi(\tilde{a}; h)^2\, d\tilde{a} = {} & \mathcal{E}h^2 a + \frac{\pi}{2}\mathcal{E}hf'(0)a^2 \\ & + \mathcal{E}\left(\frac{2}{3}hf''(0) + \frac{\pi^2}{12}f'(0)^2\right)a^3 + O(a^4).\end{aligned} \tag{A.4}$$

It follows that in the limit $(a, h) \to (0, 0)$ with $a > 0$, the potential energy can be written as

$$\begin{aligned}\Pi(a, h; \Delta) = {} & \frac{1}{2}k_s\Delta^2 - k_s\Delta h + \frac{1}{2}k_s h^2 - \pi w a^2 \\ & + \mathcal{E}h^2 a + \frac{\pi}{2}\mathcal{E}f'(0)ha^2 + \mathcal{E}\frac{\pi^2}{12}f'(0)^2 a^3 + O(\|(a, h)\|^4).\end{aligned} \tag{A.5}$$

When $(a, h) = (0, 0)$ the value of $\Pi(\cdot, \cdot; \Delta)$ equals $k_s\Delta^2/2$. Taking this into account, it follows from (A.5) that in the limit $(a, h) \to (0, 0)$ with $a > 0$,

$$\Pi(a, h; \Delta) - \Pi(0, 0; \Delta) = -k_s\Delta h + \frac{1}{2}k_s h^2 - \pi w a^2 + O(\|(a, h)\|^3). \tag{A.6}$$

First consider the case $|\Delta| \neq 0$. In this case, using (A.6), we can express that

$$\Pi(a, h; \Delta) - \Pi(0, 0; \Delta) = -k_s\Delta h + O(\|(a, h)\|^2) \tag{A.7}$$

in the limit $(a, h) \to (0, 0)$ with $a > 0$. The asymptotic expansion given by (A.7) holds for all sequences $(a_n, h_n) n \in \mathbb{N}$ converging to (0,0) in which $a_n > 0$. An example of such a sequence is $(|\Delta|/n, \Delta/n) n \in \mathbb{N}$. In this sequence, it follows from (A.7) and the definition of $O(\cdot)$ that there exists an $N \in \mathbb{N}$ such that for all $n > N$ the sign of $\Pi(a_n, h_n; \Delta) - \Pi(0, 0; \Delta)$ is the same as that of $-k_s\Delta^2/n$. Since $k_s > 0$, this result implies that no matter how small we choose δ there will always exist a point in $B(0, 0, \delta)$ where the value of $\Pi(\cdot, \cdot; \Delta)$ is smaller than its value at the point $(a, h) = (0, 0)$. This proves that when $|\Delta| \neq 0$, the point $(a, h) = (0, 0)$ cannot be a solution.

Now let us consider the case $|\Delta| = 0$. For this case, using (A.6), we can express

$$\Pi(a, h; \Delta) - \Pi(0, 0; \Delta) = \frac{1}{2}k_s h^2 - \pi w a^2 + O(\|(a, h)\|^3). \tag{A.8}$$

Consider the sequence $(a_n, h_n)_{n\in\mathbb{N}}$ when $a_n = |\Delta|/n$ and $h_n = 0$. Note that this is an admissible sequence since $a_n > 0$ for all n. For this sequence, it follows from (A.8) and the definition of $O(\cdot)$ that there exists an $N \in \mathbb{N}$ such that for all $n > N$ the sign of $\Pi(a_n, h_n; \Delta) - \Pi(0, 0; \Delta)$ is the same as that of $-\pi w\Delta^2/n^2$. Since $w > 0$, this result implies that no matter how small we choose δ there will always exist a point in $B(0, 0, \delta)$ where the value of $\Pi(\cdot, \cdot; \Delta)$ is smaller than its value at the point $(a, h) = (0, 0)$. Hence, even in the case $|\Delta| = 0$, the point $(a, h) = (0, 0)$ cannot be a solution.

Appendix B. Sign of $\chi(a; h)$

We take the negative root of $\chi(a^\circ; h^\circ)$ from (2.15b). This is because a negative sign implies tensile tractions close to the contact periphery, whereas a positive sign implies a compressive tractions close to the contact periphery. Adhesion indicates an attractive interaction between the surfaces. Thus, for the case of adhesive contact, the traction in a region close enough to the contact periphery has to be tensile when in equilibrium. The proof is as follows. According to Kesari and Lew (2012), the surface traction of the elastic half-space is

$$t_z(r, z = 0; h) = -\frac{\mathcal{E}}{2r}\frac{d}{dr}\int_r^a \frac{\chi(\tilde{a}; h)\tilde{a}}{\sqrt{\tilde{a}^2 - r^2}}\, d\tilde{a}$$

$$= -\frac{\mathcal{E}}{2r}\frac{d}{dr}\left[\chi(a;h)\sqrt{a^2-r^2} - \int_r^a \chi'(\tilde{a};h)\sqrt{\tilde{a}^2-r^2}\,d\tilde{a}\right]$$
$$= -\frac{\mathcal{E}}{2r}\left[-\chi(a;h)\frac{r}{\sqrt{a^2-r^2}} + r\int_r^a \chi'(\tilde{a};h)\sqrt{\tilde{a}^2-r^2}\,d\tilde{a}\right]$$
$$= \frac{\mathcal{E}}{2}\left[\frac{\chi(a;h)}{\sqrt{a^2-r^2}} - \int_r^a \chi'(\tilde{a};h)\sqrt{\tilde{a}^2-r^2}\,d\tilde{a}\right], \tag{B.1}$$

where $\chi'(a;h) = \partial\chi(\tilde{a};h)/\partial\tilde{a}$. Let $a = a^\circ$, $h = h^\circ$, and $r = (1-\epsilon)a^\circ$, where $\epsilon \to 0^+$. After substituting, (B.1) becomes

$$t_z((1-\epsilon)a^\circ;h^\circ) = \frac{\mathcal{E}}{2a^\circ}\left[\frac{\chi(a^\circ;h^\circ)}{\sqrt{2\epsilon}} + O(\sqrt{\epsilon})\right]. \tag{B.2}$$

If the traction close to the contact periphery has to be negative (or tensile traction according to the convention of Kesari and Lew (2012)), then it requires that $\chi(a^\circ;\,h^\circ) < 0$, i.e.,

$$\chi(a^\circ;h^\circ) = -\sqrt{\frac{8a^\circ w}{\pi\mathcal{E}}}. \tag{B.3}$$

Another reason why $\chi(a^\circ;\,h^\circ) < 0$ is that the surfaces should not intersect with each other outside of the contact region. The displacement discontinuity outside the contact region $[\tilde{u}]_z$ is Maugis (2000)

$$[\tilde{u}_z(r;h)] = -\int_a^r \frac{\chi(\tilde{a};h)}{\sqrt{r^2-\tilde{a}^2}}\,d\tilde{a}. \tag{B.4}$$

Let $a = a^\circ$, $h = h^\circ$, and $r = (1+\epsilon)a^\circ$, as $\epsilon \to 0^+$. Then, (B.4) becomes

$$[\tilde{u}_z((1+\epsilon)a^\circ;h^\circ)] = -\int_{a^\circ}^{(1+\epsilon)a^\circ} \frac{\chi(\tilde{a};h^\circ)}{\sqrt{((1+\epsilon)a^\circ)^2-\tilde{a}^2}}\,d\tilde{a}$$
$$= -\chi(a^\circ;h^\circ)\sqrt{2\epsilon} + O(\epsilon). \tag{B.5}$$

Because the surfaces do not intersect, this implies that $[\tilde{u}]_z > 0$ outside the contact region. Therefore it requires that $\chi(a^\circ;\,h^\circ) < 0$.

Appendix C. Second order necessary and sufficient conditions on interior solution points

In C.1 we present the general form of the second order necessary condition on an interior solution point $(a^*,\,h^*)$, and a second order sufficient condition that a stationary point $(a^\circ,\,h^\circ)$ needs to satisfy in order for it to be an interior solution point. Recall that a stationary point $(a^\circ,\,h^\circ)$ is an interior point that is also a root of the function (2.20). These conditions are given in terms of the second partial derivatives of $\Pi(\cdot,\,\cdot;\,\Delta)$. We derive expressions for the second partial derivatives of $\Pi(\cdot,\,\cdot;\,\Delta)$ at a stationary point in C.2. In C.3 we make use of those expressions to particularize and simplify the general conditions that we present in C.1. In this section we take $(a^*,\,h^*)$ to denote an interior solution point.

C1. General second order necessary and sufficient conditions from optimization theory

It can be shown that $\Pi(\cdot,\,\cdot;\,\Delta)$ is twice continuously differentiable on $\mathrm{int}(\mathcal{D})$. Therefore, it follows from standard non-linear optimization theory that a second order necessary condition on $(a^*,\,h^*)$ is that the value of its corresponding quadratic form is always non-negative. The quadratic form corresponding to a point $(a,\,h)$ is the function $Q(\cdot,\cdot;a,h) : \mathbb{R}^2\backslash(0,0) \to \mathbb{R}$, where

$$Q(x,y;a,h) := x^2\frac{\partial^2\Pi}{\partial a^2}(a,h;\Delta) + 2xy\frac{\partial^2\Pi}{\partial a\partial h}(a,h;\Delta) + y^2\frac{\partial^2\Pi}{\partial h^2}(a,h;\Delta). \tag{C.1}$$

The quadratic form $Q(\cdot,\,\cdot;\,a^*,\,h^*)$ is always non-negative iff

$$\frac{\partial^2\Pi}{\partial h^2}(a^*,h^*;\Delta) \geq 0, \tag{C.2a}$$

$$\frac{\partial^2\Pi}{\partial a^2}(a^*,h^*;\Delta)\frac{\partial^2\Pi}{\partial h^2}(a^*,h^*;\Delta) - \frac{\partial^2\Pi}{\partial a\partial h}(a^*,h^*;\Delta)^2 \geq 0, \tag{C.2b}$$

$$\frac{\partial^2\Pi}{\partial a^2}(a^*,h^*;\Delta) \geq 0. \tag{C.2c}$$

According to optimization theory, a sufficient condition for a stationary point (a°, h°) to be an interior solution point is that the value of its corresponding quadratic form must always be positive. The quadratic form corresponding to (a°, h°), namely $Q(\cdot, \cdot; a^\circ, h^\circ)$, is always positive iff

$$\frac{\partial^2 \Pi}{\partial a^2}(a^\circ, h^\circ; \Delta)\frac{\partial^2 \Pi}{\partial h^2}(a^\circ, h^\circ; \Delta) - \frac{\partial^2 \Pi}{\partial a \partial h}(a^\circ, h^\circ; \Delta)^2 > 0, \tag{C.3a}$$

$$\frac{\partial^2 \Pi}{\partial a^2}(a^\circ, h^\circ; \Delta) > 0. \tag{C.3b}$$

C2. Second order partial derivatives of $\Pi(\cdot, \cdot; \Delta)$ at an interior solution point

After differentiating (2.16) with respect to a and h, we find that

$$\frac{\partial^2 \Pi}{\partial a^2}(a, h; \Delta) = \frac{\pi^2 \mathcal{E}}{2}\chi(a; h)\frac{\partial \chi(a; h)}{\partial a} - 2\pi w, \tag{C.4a}$$

$$\frac{\partial^2 \Pi}{\partial a \partial h}(a, h; \Delta) = \frac{\pi^2 \mathcal{E}}{2}\chi(a; h)\frac{\partial \chi(a; h)}{\partial h}, \tag{C.4b}$$

$$\frac{\partial^2 \Pi}{\partial h^2}(a, h; \Delta) = \frac{\pi^2 \mathcal{E}}{2}\int_0^a \left\{\left(\frac{\partial \chi(\tilde{a}; h)}{\partial h}\right)^2 + \chi(\tilde{a}; h)\frac{\partial^2 \chi(\tilde{a}; h)}{\partial h^2}\right\} d\tilde{a} + k_s. \tag{C.4c}$$

It follows from (2.11) that

$$\frac{\partial \chi(\tilde{a}; h)}{\partial h} = \frac{2}{\pi}. \tag{C.5}$$

In light of (C.5), (C.4) is reduced to

$$\frac{\partial^2 \Pi}{\partial a^2}(a, h; \Delta) = \frac{\pi^2 \mathcal{E}}{2}\chi(a; h)\frac{\partial \chi(a; h)}{\partial a} - 2\pi w, \tag{C.6a}$$

$$\frac{\partial^2 \Pi}{\partial a \partial h}(a, h; \Delta) = \pi \mathcal{E}\chi(a; h), \tag{C.6b}$$

$$\frac{\partial^2 \Pi}{\partial h^2}(a, h; \Delta) = 2\mathcal{E}a + k_s. \tag{C.6c}$$

Eq. (C.6) gives the second partial derivatives of $\Pi(\cdot, \cdot; \Delta)$ at any interior point (a, h). Using (C.6) we next evaluate the second partial derivatives of $\Pi(\cdot, \cdot; \Delta)$ at a stationary point (a°, h°). To simply these derivatives, we first recall an important result discussed in Section 2.3.1, which is that

$$\chi(a^\circ; h^\circ) = -\sqrt{\frac{8a^\circ w}{\pi \mathcal{E}}}. \tag{C.7}$$

We first substitute (a, h) in (C.6) with (a°, h°). In the resulting equation, we then substitute $\chi(a^\circ; h^\circ)$ with the expression on the right side of (C.7). After simplifying, we determine that

$$\frac{\partial^2 \Pi}{\partial a^2}(a^\circ, h^\circ; \Delta) = -\sqrt{2\pi^3 a^\circ \mathcal{E} w}\left.\frac{\partial \chi(a; h)}{\partial a}\right|_{(a^\circ, h^\circ)} - 2\pi w, \tag{C.8a}$$

$$\frac{\partial^2 \Pi}{\partial a \partial h}(a^\circ, h^\circ; \Delta) = -\sqrt{8\pi a^\circ \mathcal{E} w}, \tag{C.8b}$$

$$\frac{\partial^2 \Pi}{\partial h^2}(a^\circ, h^\circ; \Delta) = 2\mathcal{E}a^\circ + k_s. \tag{C.8c}$$

Recall that by definition (a°, h°) is a root of the function (2.20). The application of the *Implicit function theorem* to function (2.20) infers the existence of the function f, which is defined in (2.21). Additionally, it implies that

$$\left.\frac{\partial \chi(a; h)}{\partial a}\right|_{(a^\circ, h^\circ)} = -\sqrt{\frac{2w}{\pi a^\circ \mathcal{E}}} - \frac{2}{\pi}f'(a^\circ). \tag{C.9}$$

We can then simplify (C.8a) to

$$\frac{\partial^2 \Pi}{\partial a^2}(a^\circ, h^\circ; \Delta) = \hbar'(a^\circ)\sqrt{8\pi a^\circ \mathcal{E} w}. \tag{C.10}$$

In summary, the second partial derivatives of $\Pi(\cdot, \cdot; \Delta)$ at an interior solution point are

$$\frac{\partial^2 \Pi}{\partial a^2}(a^\circ, h^\circ; \Delta) = \hbar'(a^\circ)\sqrt{8\pi a^\circ \mathcal{E} w}, \tag{C.11a}$$

$$\frac{\partial^2 \Pi}{\partial a \partial h}(a^\circ, h^\circ; \Delta) = -\sqrt{8\pi a^\circ \mathcal{E} w}, \tag{C.11b}$$

$$\frac{\partial^2 \Pi}{\partial h^2}(a^\circ, h^\circ; \Delta) = 2a^\circ \mathcal{E} + k_s. \tag{C.11c}$$

C3. Simplified second order necessary and sufficient conditions

C3.1. A second order sufficiency condition for stationary points

It follows from (C.11c) that $\partial^2\Pi/\partial h^2(a^\circ, h^\circ; \Delta) > 0$ at all stationary points, since at any stationary point $a^\circ > 0$ and by construction $\mathcal{E}$ and k_s are positive. Therefore, if (a°, h°) satisfies the inequality (C.3a), then it also satisfies the inequality (C.3b). Therefore, in order for a point to be a solution point, the only non-redundant sufficient condition on (a°, h°) is given by (C.3a). It follows from (C.11) that a stationary point (a°, h°) satisfies the sufficient condition (C.3a) iff

$$g(a^\circ) = \hbar'(a^\circ) - \frac{\sqrt{8\pi a^\circ \mathcal{E} w}}{2a^\circ \mathcal{E} + k_s} > 0. \tag{C.12}$$

C3.2. A second order necessary condition for interior solution points

Since an interior solution point is also a stationary point (Section 2.3.1), then we obtain from (C.11) that

$$\frac{\partial^2 \Pi}{\partial a^2}(a^*, h^*; \Delta) = \hbar'(a^*)\sqrt{8\pi a^* \mathcal{E} w}, \tag{C.13a}$$

$$\frac{\partial^2 \Pi}{\partial a \partial h}(a^*, h^*; \Delta) = -\sqrt{8\pi a^* \mathcal{E} w}, \tag{C.13b}$$

$$\frac{\partial^2 \Pi}{\partial h^2}(a^*, h^*; \Delta) = 2a^* \mathcal{E} + k_s. \tag{C.13c}$$

The necessary condition (C.2a) does not lead to any additional conditions on the interior solution point (a^*, h^*). This is because it follows from (C.13c) that at any interior solution point $\partial^2\Pi/\partial h^2(a^*, h^*; \Delta) > 0$, since at any interior solution point $a^* > 0$ and by construction $\mathcal{E}$ and k_s are positive.

It follows from (C.13) that the necessary condition (C.2b) holds iff $g(a^*) \geq 0$. The function g is defined in (2.22). If (a^*, h^*) satisfies the necessary condition (C.2b), then it also satisfies the necessary condition (C.2c). This is because if $\hbar'(a^*)$ is non-negative, then (C.13a) would imply that the necessary condition (C.2c) is satisfied.

If (a^*, h^*) satisfies the necessary condition (C.2b), then

$$g(a^*) = \hbar'(a^*) - \frac{\sqrt{8\pi a^* \mathcal{E} w}}{2a^* \mathcal{E} + k_s}$$

is non-negative and

$$\hbar'(a^*) \geq \frac{\sqrt{8\pi a^* \mathcal{E} w}}{2a^* \mathcal{E} + k_s}. \tag{C.14}$$

At any interior solution point, a^* is positive. By construction, $\mathcal{E}$ and k_s are positive and w is non-negative, thus (C.14) implies that $\hbar'(a^*)$ is non-negative.

Appendix D. Fitting contact experimental data to theory

In Section 4 we apply our model given in Section 3.1.1 to the experiments of Sun et al. (2004) and Notbohm et al. (2012). It follows from (3.4b) and (3.5b) that the measured indentation depth, h, and the contact force, P, in those experiments should satisfy

$$h = F(P; \hat{a}, \hat{P}), \tag{D.1}$$

where

$$F(P;\hat{a},\hat{P}) := \frac{4^{2/3}\hat{a}^2}{R}\left[\left(\frac{1+\sqrt{1+P/\hat{P}}}{2}\right)^{4/3} - \frac{2}{3}\left(\frac{1+\sqrt{1+P/\hat{P}}}{2}\right)^{1/3}\right],$$

and

$$\hat{a} := (9\pi w R^2/8\mathcal{E})^{1/3}, \tag{D.2a}$$

$$\hat{P} := 3\pi w R/2. \tag{D.2b}$$

Say (h_i, P_i), $i = 1, 2, \ldots, n$, where n is a positive integer, is a sequence of indentation depth–contact force measurements. An estimate of the mismatch between the theory and experimental results can be

$$S(\hat{a},\hat{P}) := \sum_{i=1}^{n} r_i(\hat{a},\hat{P})^2, \tag{D.3}$$

where

$$r_i(\hat{a},\hat{P}) := h_i - F(P_i;\hat{a},\hat{P}), \tag{D.4}$$

and $i = 1, 2, \ldots, n$. We take the best values for the parameters $\hat{a}$ and $\hat{P}$ to be those at which S attains its minimum. Denoting the best fit values of $\hat{a}$ and $\hat{P}$ as $\hat{a}^*$ and $\hat{P}^*$, respectively, a necessary condition that S attains its minimum at $(\hat{a}^*, \hat{P}^*)$ is that

$$\frac{\partial S}{\partial \hat{a}}(\hat{a}^*,\hat{P}^*) = 0, \tag{D.5a}$$

$$\frac{\partial S}{\partial \hat{P}}(\hat{a}^*,\hat{P}^*) = 0. \tag{D.5b}$$

We obtain $\hat{a}^*$ and $\hat{P}^*$ by numerically solving (D.5a) and (D.5b), which are a pair of coupled, nonlinear algebraic equations. The best fit values for w and $\mathcal{E}$ are then obtained by simultaneously solving (D.2a) and (D.2b) for w and $\mathcal{E}$ after first replacing in them $\hat{a}$ and $\hat{P}$ with their respective best fit values and R with its experimentally reported value.

References

Ahn, D., Shull, K.R., 1996. JKR studies of acrylic elastomer adhesion to glassy polymer substrates. Macromolecules 29 (12), 4381–4390.
Argatov, I., Li, Q., Pohrt, R., Popov, V.L., 2016. Johnson–Kendall–Roberts adhesive contact for a toroidal indenter. Proc. R. Soc. A 472 (2191), 20160218.
Arzt, E., Gorb, S., Spolenak, R., 2003. From micro to nano contacts in biological attachment devices. Proc. Natl. Acad. Sci. 100 (19), 10603–10606.
Bouchonville, N., Meyer, M., Gaude, C., Gay, E., Ratel, D., Nicolas, A., 2016. AFM mapping of the elastic properties of brain tissue reveals kpa μm^{-1} gradients of rigidity. Soft Matter 12 (29), 6232–6239.
Bradley, R.S., 1932. The cohesive force between solid surfaces and the surface energy of solids. Lond. EdinburghDublin Philos. Mag. J. Sci. 13 (86), 853–862.
Bullock, J.M., Federle, W., 2011. Beetle adhesive hairs differ in stiffness and stickiness: in vivo adhesion measurements on individual setae. Naturwissenschaften 98 (5), 381–387.
Cao, Z., Wang, P., Gao, W., Tao, L., Suk, J., Ruoff, R., Akinwande, D., Huang, R., Liechti, K., 2014. A blister test for interfacial adhesion of large-scale transferred graphene. Carbon 69, 390–400.
Cohen, T., Chan, C.U., Mahadevan, L., 2018. Competing failure modes in finite adhesive pads. Soft Matter 14 (10), 1771–1779.
Deng, W., Kesari, H., 2017. Molecular statics study of depth-dependent hysteresis in nano-scale adhesive elastic contacts. Model. Simul. Mater. Sci. Eng. 25 (5), 055002.
Deng, W., Kesari, H., 2019. Depth-dependent hysteresis in adhesive elastic contacts at large surface roughness. Sci. Rep. 9 (1), 1639.
Ebenstein, D.M., Pruitt, L.A., 2006. Nanoindentation of biological materials. Nano Today 1 (3), 26–33.
Ebenstein, D.M., Wahl, K.J., 2006. A comparison of JKR-based methods to analyze quasi-static and dynamic indentation force curves. J. Colloid Interface Sci. 298 (2), 652–662.
Eisner, T., Aneshansley, D.J., 2000. Defense by foot adhesion in a beetle (hemisphaerota cyanea). Proc. Natl. Acad. Sci. 97 (12), 6568–6573.
Friedrich, K., 2012. Friction and Wear of Polymer Composites, 1. Elsevier.
Frost, F., Gorb, S.N., Wolff, J.O., 2018. Adhesion and friction in hunting spiders: the effect of contact splitting on their attachment ability. Zool. Anz. 273, 231–239.
Hinkley, J., 1983. A blister test for adhesion of polymer films to SiO_2. J. Adhes. 16 (2), 115–125.
Huber, G., Gorb, S.N., Hosoda, N., Spolenak, R., Arzt, E., 2007. Influence of surface roughness on gecko adhesion. Acta Biomater. 3 (4), 607–610.
Hutchings, I., Shipway, P., 2017. Tribology: Friction and Wear of Engineering Materials. Butterworth-Heinemann.
Israelachvili, J.N., 2011. Intermolecular and Surface Forces. Academic press.
Johnson, K., Kendall, K., Roberts, A., 1971. Surface energy and the contact of elastic solids. Proc. R. Soc. Lond. A 324 (1558), 301–313.
Kendall, K., 1971. The adhesion and surface energy of elastic solids. J. Phys. D 4 (8), 1186.
Kendall, K., 2001. Molecular Adhesion and its Applications: The Sticky Universe. Springer, US.
Kesari, H., Doll, J.C., Pruitt, B.L., Cai, W., Lew, A.J., 2010. Role of surface roughness in hysteresis during adhesive elastic contact. Philos. Mag. Lett. 90 (12), 891–902.
Kesari, H., Lew, A.J., 2011. Effective macroscopic adhesive contact behavior induced by small surface roughness. J. Mech. Phys. Solids 59 (12), 2488–2510.
Kesari, H., Lew, A.J., 2012. Adhesive frictionless contact between an elastic isotropic half-space and a rigid axi-symmetric punch. J. Elast. 106 (2), 203–224.
Kim, J., Kim, K., Kim, Y., 1989. Mechanical effects in peel adhesion test. J. Adhes. Sci. Technol. 3 (1), 175–187.
Maugis, D., 2000. Contact Adhesion and Rupture of Elastic Solids. Solid State Sciences. Springer.
Notbohm, J., Poon, B., Ravichandran, G., 2012. Analysis of nanoindentation of soft materials with an atomic force microscope. J. Mater. Res. 27 (1), 229–237.
Popov, V.L., Pohrt, R., Li, Q., 2017. Strength of adhesive contacts: influence of contact geometry and material gradients. Friction 5 (3), 308–325.

Sneddon, I.N., 1965. The relation between load and penetration in the axisymmetric Boussinesq problem for a punch of arbitrary profile. Int. J. Eng. Sci. 3 (1), 47–57.
Sun, Y., Akhremitchev, B., Walker, G.C., 2004. Using the adhesive interaction between atomic force microscopy tips and polymer surfaces to measure the elastic modulus of compliant samples. Langmuir 20 (14), 5837–5845.
Takahashi, K., Mizuno, R., Onzawa, T., 1995. Influence of the stiffness of the measurement system on the elastic adhesional contact. J. Adhes. Sci. Technol. 9 (11), 1451–1464.
Tanner, D.M., Smith, N.F., Irwin, L.W., Eaton, W.P., Helgesen, K.S., Clement, J.J., Miller, W.M., Miller, S.L., Dugger, M.T., Walraven, J.A., Peterson, K.A., 2000. MEMS Reliability: Infrastructure, Test Structures, Experiments, and Failure Modes. Technical Report. Sandia National Labs., Albuquerque, NM (US); Sandia National Labs., Livermore, CA (US).
Willert, E., Li, Q., Popov, V.L., 2016. The JKR-adhesive normal contact problem of axisymmetric rigid punches with a flat annular shape or concave profiles. Facta Univ. Ser. 14 (3), 281–292.
Wolff, J.O., Gorb, S.N., 2012. Surface roughness effects on attachment ability of the spider philodromus dispar (araneae, philodromidae). J. Exp. Biol. 215 (1), 179–184.
Yang, F., 2003. Load–displacement relation in adhesion measurement. J. Phys. D 36 (19), 2417.